

1 Deciphering relationships between the Nicobar and Bengal Submarine Fans, Indian Ocean

2

3 Kevin T. Pickering <sup>1</sup>, Andrew Carter <sup>2</sup>, Sergio Andò <sup>3</sup>, Eduardo Garzanti <sup>4</sup>, Mara Limonta <sup>4</sup>,

4 Giovanni Vezzoli <sup>4</sup>, Kitty L. Milliken <sup>5</sup>

5

6 <sup>1</sup> Earth Sciences, University College London (UCL), London WC1E 6BT, UK

7 [kt.pickering@ucl.ac.uk](mailto:kt.pickering@ucl.ac.uk)

8

9 <sup>2</sup> Dept of Earth and Planetary Sciences, Birkbeck, University of London, Malet Street,

10 Bloomsbury, London WC1E 7HX

11 [a.carter@ucl.ac.uk](mailto:a.carter@ucl.ac.uk)

12

13 <sup>3</sup> Laboratory for Provenance Studies, Department of Earth and Environmental Sciences,

14 University of Milano-Bicocca, 210126 Milano, Italy

15 [sergio.ando@unimib.it](mailto:sergio.ando@unimib.it)

16 [eduardo.garzanti@unimib.it](mailto:eduardo.garzanti@unimib.it)

17 [mara.limonta@unimib.it](mailto:mara.limonta@unimib.it)

18 [giovanni.vezzoli@unimib.it](mailto:giovanni.vezzoli@unimib.it)

19

20 <sup>4</sup> Bureau of Economic Geology, Jackson School of Geosciences, The University of Texas at

21 Austin, 2305 Speedway Stop C1160 Austin, TX 78712-1692, USA

22 [kittym@utexas.edu](mailto:kittym@utexas.edu)

23

24 Keywords: Nicobar Fan, Bengal Fan, sediment provenance, IODP Expedition 362, Indian Ocean,

25 Sunda Subduction Zone

26

27

## 28 Abstract

29 The Nicobar Fan and Bengal fans can be considered as the eastern and western parts,  
30 respectively, of the largest submarine-fan system in the world. This study presents the integrated  
31 results of petrographic and provenance studies from the Nicobar Fan and evaluates these in the  
32 context of controls on sedimentation. Both fans were predominantly supplied by Himalaya-  
33 derived material from the main tectono-stratigraphic sequences as well as the Gangdese arc. A  
34 lack of volcanic material in the Nicobar Fan rules out sources from the Sumatra magmatic arc.  
35 Overall, the petrographic data shows a progressive decrease in sedimentary detritus and  
36 corresponding increase of higher-grade metamorphic detritus up-section. Changes in sediment  
37 provenance and exhumation rates in the Himalaya are seen to track changes in sediment  
38 accumulation rates. High sediment accumulation rates in the Bengal Fan occurred at ~13.5–8.3  
39 Ma, and in the Nicobar Fan from ~9.5–5 Ma. Both fans show peak accumulation rates at 9.5–8.3  
40 Ma (but with the Nicobar Fan being about twice as high), and both record a sharp drop from  
41 ~5.5–5.2 Ma, that coincided with a change in river drainage associated with the Brahmaputra  
42 River diverting west of the uplifting Shillong Plateau. At ~5 Ma, the Nicobar Fan was supplied  
43 by an eastern drainage route that finally closed at ~2 Ma, when sediment accumulation rates in  
44 the Nicobar Fan significantly decreased. Sediment provenance record these changes in routing  
45 whereby Bengal Fan deposits include granitoid sources from the Namche Barwa massif in the  
46 eastern syntaxis that are not seen in the Nicobar Fan, likely due to a more localised eastern  
47 drainage that included material from the Indo-Burman wedge. Prior to ~3 Ma, source exhumation  
48 rates were rapid and constant and the short lag-time rules out significant intermediate storage and  
49 mixing. In terms of climate *versus* tectonic controls, tectonically driven changes in the river  
50 network have had most influence on fan sedimentation.

51

## 52 1. Introduction

53

54           The Bengal–Nicobar Fan, Indian Ocean (Fig. 1), has the greatest length and area of any  
55 submarine fan worldwide, and has been intensively studied to investigate the possible link  
56 between Himalayan and southeast Asian tectonics, and the Asian monsoon (Curry and Moore,  
57 1971; France-Lanord *et al.*, 2016). International Ocean Discovery Program (IODP) Expedition  
58 362 sampled the full sedimentary succession of the Nicobar Fan west of North Sumatra (Fig. 1).  
59 This work showed that starting at ~9.5 Ma, there was a dramatic and sustained rise in sediment  
60 accumulation rates (SARs) from 250–350 m/Myr until ~2 Ma that equalled or far exceeded those  
61 on the Bengal Fan at similar latitudes (McNeill *et al.*, 2017a,b). This rise in SARs and a constant  
62 Himalayan-derived provenance indicates a major restructuring of the sediment routing in the  
63 Bengal–Nicobar submarine fan that was interpreted as coinciding with the uplift of the eastern  
64 Himalaya and Shillong Plateau and encroachment of the west-propagating Indo–Burmese wedge,  
65 reducing continental accommodation space and increasing sediment supply directly to the fan  
66 (*ibid.*). These results challenged the commonly held view that discrete tectonic or climatic events  
67 that impacted on the Himalayan–Tibetan Plateau caused the changes in sediment flux seen in the  
68 Bengal submarine fan.

69           A provenance contribution for the sediment gravity flow sandy deposits (SGF;  
70 terminology after Pickering and Hiscott, 2016) from the only previously drilled submarine fan in  
71 the eastern Indian Ocean (DSDP Site 211; referred to as the “Investigator Fan”, from the Sunda  
72 arc in the vicinity of the Andaman–Nicobar islands) cannot be entirely ruled out. However, the  
73 indistinguishable nature of the sands from DSDP sites 211 and 218 (the latter being Bengal Fan  
74 deposits) suggests that they were derived from the same Himalayan source (Ingersoll and Suczek,  
75 1979). Lithic populations of Bengal–Nicobar sands are dominated by metasedimentary rock  
76 types, with the abundant micas (predominantly muscovite and biotite), suggesting a provenance  
77 from uplifted crystalline basement terranes of granitic to granodioritic composition, as well as  
78 extensive low- to high-grade metasedimentary terranes (Ingersoll and Suczek, 1979). The

79 Investigator Fan was likely a distal fan setting and, because of subduction-accretion processes,  
80 now an isolated segment of the Nicobar Fan. The oldest recovered fan sediments are ~19 Ma  
81 mud-rich SGF deposits (Pickering *et al.*, 2019).

82 Here, we present the integrated results of studies on sediments from the Nicobar Fan, and  
83 evaluate these in the context of siliciclastic sediment provenance both to the Bengal and Nicobar  
84 fans. Figure 2 shows the potential source areas for the sediments that are considered in this paper,  
85 and Figure 3 summarises the stratigraphic units defined from IODP Expedition 362.

86 In order to better understand sediment source and variations in sediment flux through time  
87 and build on the initial findings of the study by McNeill *et al.* (2017b), we conducted a more  
88 extensive analysis of IODP 362 samples from sites U1480 (Fig. 3) and U1481 that extend back to  
89 15 Ma. In addition to detrital zircon U–Pb and heavy mineral and petrographic analyses, we also  
90 applied detrital apatite fission track analysis to examine bedrock exhumation rates as this can  
91 help pinpoint sediment source areas. Detrital zircon U–Pb and apatite fission track (AFT)  
92 analyses were performed at the London Geochronology Centre at University College London,  
93 U.K. and heavy mineral and petrography data were analysed by the team at the Laboratory for  
94 Provenance Studies, University of Milano–Bicocca, Italy. Full method details are provided in the  
95 supplementary sections.

96

### 97 3. RESULTS

98

99 In this section, we highlight the main trends observed in the datasets. More complete  
100 descriptions of the data are provided in the Supplementary section.

101

#### 102 3.1. Petrography

103 Provenance interpretation based on composition alone is made difficult by potential  
104 influences of grain size, hydraulic sorting and modification by diagenesis (Ando *et al.*, 2012).

105 These potential influences are considered in relation to compositional trends. The succession in  
106 the Nicobar Fan can be subdivided in four petrofacies intervals (Fig. 4 and Supplementary data),  
107 from top to bottom: Petrofacies A (age < 2.39 Ma) consists of upper fine-grained feldspatho-  
108 quartzose sand rich in plagioclase and heavy minerals; Petrofacies B (age between 8.2–2.39 Ma)  
109 consists of fine-grained feldspatho-quartzose to quartz-rich feldspatho- quartzose sand;  
110 Petrofacies C (age 8.2 Ma) consists of fine-grained litho-feldspatho-quartzose to quartz-rich  
111 feldspatho-quartzose sand with more sedimentary and low-rank metasedimentary lithic grains;  
112 Petrofacies D (age > 8.2 Ma) is finer-grained and rich in feldspatho-litho-quartzose sands, and  
113 low-rank metasedimentary rock fragments.

114         Analysed samples are all fine-grained sands showing a coarsening-upward trend.  
115 Composition ranges from feldspatho-litho-quartzose to quartz-rich feldspatho-quartzose (Fig. 4).  
116 Metamorphic rock fragments include quartz-mica, slate, quartz-sericite, phyllite, schist, and rare  
117 garnet-bearing or sillimanite-bearing schist and gneiss. Subordinate fragments include granitoids  
118 and sedimentary rocks (i.e., shale, sparite, dolomite, siltstone, chert, micrite). Volcanic,  
119 metavolcanic, metabasite, and ultramafic lithics are rare. Among accessory grains, biotite and  
120 subordinate muscovite are invariably common, representing together  $11 \pm 5$  % of total framework  
121 grains. Heavy-mineral concentration estimated by point-counting ranges from 0.6–4%.

122         Average compositions are not significantly different throughout the sampled cores, but  
123 there are some noteworthy differences in volume percentages of total (HMC) and transparent  
124 (tHMC) heavy minerals. Moderately rich amphibole-epidote-garnet assemblages are present in  
125 the upper part of the IODP Site 1480 core (< 8.2 Ma), with the highest relative abundance (Amp  
126 59–65% tHMC) seen in samples 80F9 and 80F52 (3.8–1.98 Ma). By contrast, epidote-  
127 amphibole-garnet assemblages are poor in the lower part of IODP sites 1480 and 1481 (10–8.2  
128 Ma). Both cores record minor levels of apatite, tourmaline, sillimanite, clinopyroxene, zircon,  
129 titanite, staurolite, kyanite, rutile, and rare chloritoid apart from the lower part of IODP sites 1480  
130 and 1481 where tourmaline and apatite are common. Average indices for IODP samples < 8.2 Ma

131 (sites 1480 and 1481) are tHMC (transparent Heavy Mineral Concentration)  $4.0 \pm 1.4$ , a ZTR  
132  $6 \pm 3$  (Zircon-Tourmaline-Rutile index), HCI (Hornblende Colour Index) index  $5 \pm 2$ , and  
133 Metasedimentary Minerals Index (MMI)  $63 \pm 16$ . Broadly similar average values were measured  
134 in the older samples (10–8.2 Ma) from sites 1480 and 1481; tHMC,  $1.9 \pm 0.9$ , the ZTR  $11 \pm 5$ , the  
135 HCI  $8 \pm 3$ , and the MMI index  $37 \pm 19$ . Within samples the down-section decrease in MMI index  
136 and increase in the ZTR index ( $r = 0.74$  and  $0.66$ ) is a typical mineralogical feature of Himalayan-  
137 derived foreland-basin sediments (e.g., Szulc *et al.*, 2006; Najman *et al.*, 2012).

138 Both hydraulic-sorting processes and diagenesis may alter provenance signals. IODP Leg  
139 362 core depths reached  $\sim 1,350$  mbsf sufficient to observe diagenetic alteration and certain  
140 features are consistent with this including a progressive decrease in tHMC index with burial  
141 depth, from 4 to 1. Amphibole decreases from  $\sim 50\%$  tHM to  $\sim 15\%$ , while epidote increases from  
142  $\leq 20$  to  $48\%$  tHM. Sillimanite becomes rare to absent at greater burial depths. Conversely, zircon,  
143 tourmaline, apatite, and chloritoid increase. However, not all minerals show the expected trends  
144 associated with diagenesis. Garnet, kyanite, staurolite, titanite, and rutile do not show significant  
145 changes with burial depth. If diagenetic alteration were important, garnet concentrations would  
146 be expected to increase. A grain-size increase is observed throughout the section and a good  
147 positive correlation is observed between grain size and heavy-mineral concentration ( $r = 0.79$ ,  
148 significance level 0.1%). Garnet correlates positively with grain size both in the upper part of  
149 IODP Site 1480 core ( $r = 0.72$ , significance level. 5%) and in the lower part of both IODP sites  
150 1480 and 1481 ( $r = 0.81$ , significance level. 2%). Conversely, epidote reaches a maximum in the  
151 finest-grained sample 81A22 ( $\sim 9.5$ – $8.5$  Ma), which is the sample with lowest heavy-mineral  
152 concentration. We interpret that the epidote/garnet ratio was controlled by grain size and  
153 hydraulic-sorting processes rather than diagenesis.

154 Whilst the epidote/garnet ratio has been considered as a useful parameter to distinguish  
155 between Ganges and Brahmaputra river sediments (Heroy *et al.*, 2003; Garzanti *et al.*, 2010), it is  
156 not possible to definitely identify changes in contributions from either the Ganges or

157 Brahmaputra because of these grain-size effects. After integrating petrographic and heavy-  
158 mineral evidence, the most reasonable conclusion is that vertical compositional trends show the  
159 effect of both provenance change and diagenetic bias. However, the data clearly show a  
160 progressive decrease in sedimentary detritus and corresponding up-section increase of higher-  
161 grade metamorphic detritus in the last 5.5 Ma, consistent with an increasing contribution from  
162 metamorphic source rocks found in the Greater Himalayan domain.. The Sumatra magmatic arc  
163 is an unpalatable candidate, because volcanic detritus remains very minor even in Petrofacies D.  
164 To gain more insight into sand provenance we examined detrital zircon U-Pb and detrital apatite  
165 fission track signatures.

166

### 167 3.2. Detrital zircon U–Pb analysis

168 In total 32 samples were analyzed covering the time interval between 15.4–0.21 Ma. Most  
169 samples contained sufficient zircon to measure > 100 grain ages, enough to detect the main  
170 detrital age components (Table S1). Figures 5 and 6 present the data in the form of Kernel density  
171 estimates (KDE plots) and multidimensional scaling maps (Vermeesch, 2013) based on  
172 calculated K–S distances between U–Pb age spectra, comparing Nicobar Fan sand samples from  
173 this study with possible source areas compiled from the literature (Campbell *et al.*, 2005; Allen *et*  
174 *al.*, 2008; Bracciali *et al.*, 2016 and references therein; Gehrels *et al.*, 2011; Limonta *et al.*, 2017).  
175 Although potential source areas span the drainage network of the Ganges and Brahmaputra  
176 rivers, the Brahmaputra River is considered more important as the upper Yarlung-Brahmaputra  
177 River extends into the Lhasa terrane on the Tibetan Plateau that consists of Cambrian-age  
178 granites, and Paleozoic and Mesozoic clastics intruded by Jurassic through Paleogene granitoids  
179 of the Gangdese Arc as well as younger magmatism associated with partial melting of thickened  
180 lower crust (Ji *et al.*, 2019). Southwards of the Indus-Yarlung suture zone are the main tectono-  
181 stratigraphic sequences of Himalayan rocks represented by (from north to south) Paleozoic and  
182 Mesozoic sedimentary rocks of the Tethyan Himalaya Sequence (THS), Late Neoproterozoic to

183 Ordovician high-grade metamorphic and plutonic rocks of the Greater Himalaya Sequence (GHS)  
184 and Paleoproterozoic and older metasedimentary and igneous rocks of the Lesser Himalaya  
185 Sequence (LHS). Neogene leucogranites span both the THS and GHS. The southernmost unit  
186 comprises Neogene foreland-basin sediments, such as the Siwaliks (DeCelles *et al.*, 1998;  
187 Najman & Garzanti, 2000)

188         McNeill *et al.* (2017b) proposed that the Nicobar Fan results show a provenance from  
189 Brahmaputra River sands mixed with reworked Himalaya material originally deposited in the  
190 remnant ocean and Surma Basin (Fig. 2). A detrital zircon U–Pb study of Bengal Fan sands from  
191 IODP 354 by Blum *et al.* (2018) indicated Himalayan sources that included the eastern syntaxis,  
192 but few samples could be interpreted as representing a Ganges or Brahmaputra provenance end-  
193 member: most samples could be explained by mixing between both river systems. Figure 5  
194 compares KDE plots of detrital zircon U–Pb data from the Bengal Fan (Blum *et al.*, 2018) and  
195 Nicobar Fan (this study). The two datasets share Himalayan sources, and visually the age  
196 distributions appear similar. A more robust way to compare the age distributions are  
197 multidimensional scaling maps (MDS, Vermeesch, 2013), based on calculated K–S distances  
198 between U–Pb age spectra. If the Nicobar Fan sediments were simply the result of switching and  
199 mixing of the two river feeder systems, the MDS map would not show any major differences  
200 between Nicobar and Bengal Fan samples.

201         The MDS map in Figure 6A compares both the Nicobar and Bengal Fan datasets, together  
202 with modern sands from the Ganges and Brahmaputra rivers. This map shows that the two fans  
203 plot separately with little overlap. Nicobar Fan samples show greater spread in the Y-axis  
204 compared to the Bengal Fan suggesting input from additional sources to those of the Bengal Fan.  
205 Blum *et al.* (2018) suggested that the Plio-Pleistocene Ganges and Brahmaputra delivered sand to  
206 the delta independently but were later mixed, by delta-plain avulsions (including on the inner  
207 shelf delta during highstands), longshore drift or submarine gravity flows. The Bengal Fan data  
208 plot support mixing although most samples show a closer affinity to the Brahmaputra River

209 especially samples  $\leq 3.2$  Ma. The KDE plots show fans share the same range of Himalayan  
210 source ages (Fig. 2) differing mainly in the proportions of source ages (mainly GHS, THS, LHS).  
211 A few of the youngest Bengal Fan sediments contain ages  $< 10$  Ma, diagnostic of the syntaxis  
212 region (Booth *et al.*, 2004) that are missing from Nicobar Fan samples. Whilst similar ages can be  
213 found in the Lhasa terrane, Najman *et al.* (2019) ruled this out by using zircon fission track and  
214 rutile U-Pb ages to differentiate between syntaxial- and non-syntaxial-derived grains.  
215 Proterozoic-aged zircons are common in the Miocene Bengal Fan samples and fit with a more  
216 constant contribution (albeit low) from LHS/Ganges sources compared to the Nicobar Fan.

217 To further explore differences between the Bengal and Nicobar Fan zircon data, Figure  
218 6B shows an MDS map that includes zircons from Oligocene–Pleistocene samples of the Surma  
219 Basin (peripheral Indo–Burma wedge). The Surma Basin tectono-stratigraphic units (from old to  
220 young; Barail, Bhuban, Bokabil, Tipam and Dupi Tila) share a Himalayan provenance (Najman  
221 *et al.*, 2008) dominated by GHS and Trans-Himalayan arc detritus with minor contributions from  
222 the LHS (especially in the Dupi Tila), ophiolite, and possibly the eastern Himalayan or Lohit–  
223 Dianxi (Burma) batholiths (Najman *et al.*, 2012; Bracciali *et al.*, 2016). Also included are  
224 combined samples from the Himalayan foreland basin section at Dungsam Chu, eastern Bhutan,  
225 that are considered to represent paleo-Brahmaputra deposited after the uplift of the Shillong  
226 Plateau that caused the river to re-route to the north and west (Govin *et al.* 2018). The MDS  
227 graph (Fig. 6A) shows that samples from both fans plot in common space until a group of young  
228 Bengal Fan samples ( $< 3.2$  Ma) plotting lower down on the Y-axis along with the modern  
229 Brahmaputra. The MDS graph in (Fig. 6C) shows the same trend. The ages of the Surma Basin  
230 units plot within the fields for both fans. To understand the nature of differences on the MDS  
231 graph Figure 6D compares the normalised percent contributions of the same age groups used by  
232 Blum *et al.* (2018), thereby permitting direct comparison with the Bengal Fan samples. The  
233 percentages are remarkably similar given the data were produced using different experimental  
234 procedures, but there are some subtle differences that help explain the MDS graphs. For example,

235 the Nicobar Fan samples show a consistently higher proportion of ages between 400–600 Ma,  
236 typical of the GHS. Figure 6B shows that the Bengal Fan samples with ages < 4 Ma contain a  
237 significantly higher percentage of young grain ages (up to 13% compared to < 3 % in the Nicobar  
238 Fan), which can explain the trend of young (< 3.2 Ma) Bengal Fan samples.

239

### 240 3.3 Detrital apatite fission track data

241 Apatite fission track (AFT) data can help discern source areas, as AFT exhumation ages  
242 are known to vary across the Himalayan arc (Thiede and Ehlers, 2013). Table 1 summarises the  
243 detrital fission apatite fission track results. The raw data and analytical details are provided in the  
244 Supplementary section. Sample burial depths (max. 1,350 mbsf) and downhole temperatures rule  
245 out post-depositional resetting confirmed by ages older or contemporaneous with deposition age,  
246 hence the data reflect provenance. The numbers of measured grain ages varied due to abundances  
247 of suitable apatite. In most cases, however, there were sufficient numbers of grains to define the  
248 principal age component quantified using the minimum age model based on a four-parameter  
249 probability distribution (Galbraith, 2005), implemented in DensityPlotter (Vermeesch, 2012). The  
250 minimum age is a more robust indicator of youngest age components where single grain  
251 spontaneous tracks have zero or low track counts. Grain counts were pooled together for samples  
252 with the same or similar deposition ages. Figure 7 is a plot of lag-time between sample  
253 depositional age and AFT age components each diagnostic of the time taken for exhumation,  
254 routing and deposition within the Nicobar Fan. The main population of apatites in all samples  
255 show a younging trend with a near to constant lag time of 1–2 Myr that records rapid exhumation  
256 in the apatite source areas. This pattern rules out significant intermediate storage prior to  
257 deposition within the Nicobar Fan. The second most abundant population of Miocene age also  
258 shows a constant younging trend. Together these data show that there was very little mixing  
259 occurring within the submarine fan. If this were the case the age that components of older  
260 samples would also be present in younger sands and there would not be any systematic trend.

261 Older grains with ages between  $35\pm 10$  and  $337\pm 65$  Ma were also present in some samples  
262 mostly represented by single grains. Also shown Table 1, the main populations of apatites found  
263 in unreset Plio–Pleistocene foreland basins that characterize bedrock exhumation (mainly GHS as  
264 apatite is uncommon in LHS rocks) at the time they were deposited (Chirouze *et al.*, 2013;  
265 Coutand *et al.*, 2016). In all cases these data are closely similar to the dominant minimum age  
266 population seen in fan samples of equivalent deposition age.

267

#### 268 4. Discussion

269 Compositional data confirm that the Nicobar Fan was a major sink for Himalaya-derived  
270 material since the Miocene. Vertical compositional trends show the effect of both provenance  
271 change and diagenetic bias due to dissolution of less durable detrital minerals as well as grain  
272 size and hydraulic-sorting processes (see Supplementary section for further details). As a  
273 consequence more durable heavy minerals, including zircon, tourmaline, apatite, garnet and  
274 epidote tend to be relatively enriched with increasing age and burial depth. Epidote tends to  
275 increase in finer-grained samples and where heavy-mineral concentration is lower, and likewise  
276 garnet increases in coarser-grained samples and where heavy-mineral concentration is higher.  
277 Despite such influences there is a clear upward increase in higher-grade metamorphic detritus  
278 from  $\sim 5.5$  Ma (mainly hornblende, epidote, garnet, apatite, clinopyroxene, tourmaline,  
279 sillimanite, kyanite, zircon, titanite, and rare staurolite and rutile) consistent with Himalayan  
280 sources. The origin of sedimentary to low-grade metasedimentary detritus, the importance of  
281 which decreases progressively upwards, has yet to be ascertained, and the rare volcanic detritus  
282 rules out the Sumatra magmatic arc as a major contributor. Petrographic data suggests that sandy  
283 sediments reaching the Bengal shelf, and the Bengal and Nicobar fans, most closely match in  
284 composition those of the Brahmaputra sediments (Thompson, 1974; Ingersoll and Suczek, 1979;  
285 Yokohama *et al.*, 1990; Garzanti, 2019).

286 Comparison of Bengal and Nicobar Fan detrital zircon datasets showed they share the  
287 same range of Himalayan source ages (Fig. 2) but there are also differences. Some Bengal Fan  
288 samples included ages  $< 10$  Ma diagnostic of the syntaxis region (Booth *et al.*, 2004) that are  
289 missing from the Nicobar Fan This absence is unlikely to be a sampling artifact given that  $>100$   
290 grain ages were measured in most samples, which gives a 95% certainty that no fraction of a  
291 population is missed. Proterozoic-aged zircons are more common in Bengal Fan samples and fit  
292 with a more constant contribution from LHS and Ganges sources. Combined U–Pb and  
293 thermochronometry work on the Bengal Fan samples (Najman *et al.*, 2019) also found a  
294 significant component of grains derived from the TransHimalaya, supplied by drainages  
295 associated with the upper reaches of the Yarlung–Brahmaputra River in addition to some  
296 contribution from erosion of the Indo–Burma ranges. Whilst this background signal was present  
297 throughout the drilled section of the Bengal Fan, notable differences in proportions of zircon ages  
298 were considered to reflect differences in the loci of sediment production possibly driven by  
299 climate change. The same could also be argued for the Nicobar Fan.

300 Both the Bengal and Nicobar fans show significant temporal changes in sediment  
301 accumulation rates. The changes, however, are not always synchronous, as seen in Figure 8 that  
302 compares sediment mass accumulation rates (MARs) for the two systems (after Pickering *et al.*,  
303 2019). Mass accumulation rate (MAR) is related to the equation and calculations given in  
304 Pickering *et al.* (2019), whereas sediment accumulation rate (SAR) is used in this paper as a more  
305 general term. Whilst avulsion processes on the fans might account for some of the differences, we  
306 believe that a comparison of MARs from the Bengal and Nicobar fans is reasonable, because  
307 IODP Site U1451 (Bengal Fan) and IODP Site U1480 (Nicobar Fan) were drilled at comparable  
308 distances from the main sediment source, in similar latitudes, in similar fan environments, at a  
309 distance west of the NinetyEast Ridge that compares well with IODP Site 362 east of the ridge.  
310 Also, IODP Site U1451 penetrated  $\sim 300$  m deeper than any other site on the Bengal Fan, and has  
311 the most complete stratigraphic record (and with greater core recovery, i.e., 86% with 337.80 m

312 core recovered in Hole U1451A *versus* 64% with 282.73 m core recovered in Hole U1450A, then  
313 29% with 180.86 m core recovered in Hole U1451A *versus* 23% with 46.67 m core recovered in  
314 Hole U1450A: see table 1 in IODP 354 Preliminary Report, 2015). Significant sediment mass  
315 accumulation rates occurred earlier in the Bengal Fan (from ~13.5– 8.3 Ma), with peak MARs  
316 reached in both fans over the same time interval, from ~9.5–8.3 Ma. However, between ~5–9.5  
317 Ma, MARs appears significantly higher in the Nicobar Fan (Fig. 8). Similarly both fans show a  
318 marked fall in MARs at ~5.5–5.2 Ma. After this, MARs in the Bengal Fan remained low but in  
319 the Nicobar Fan they increased again from ~3.8 Ma and peaked between ~2.4–1.6 Ma, after  
320 which accumulation dramatically dropped to low rates until a small rise in the Late Pleistocene,  
321 that is also seen in the Bengal Fan. The two major changes seen in both fans thus took place at  
322 9.5–8.3 Ma and 5.5–5.2 Ma, suggesting a common mechanism. We now explore if these changes  
323 can be linked with any obvious climatic events.

324

#### 325 4.1 Influence of Climate

326 Following the end of the Middle Miocene climatic optimum (a period of relative warmth  
327 from 18–14 Ma), the deep-marine composite isotope compilation shows that the  $\delta^{18}\text{O}$  record was  
328 characterised by a series of incremental steps at ~14.6, 13.9, 13.1, 10.6, 9.9, and 9.0 Ma, which  
329 have been attributed to progressive deep-water (high-latitude) cooling and/or glaciation  
330 (Holbourn *et al.*, 2013). The earlier part of this step-wise deterioration in global climate therefore  
331 includes the Nicobar Fan, with the so-called Late Miocene “*Carbonate Crash*” at ~11–9 Ma  
332 (Lyle *et al.*, 2008). A high-resolution benthic isotope record, combined with paired mixed-layer  
333 isotope and Mg/Ca-derived temperature data by Holbourn *et al.* (2018) show that a long-term  
334 cooling trend was synchronous with the intensification of the Asian winter monsoon and  
335 strengthening of the biological pump from ~7–5.5 Ma. The climate shift occurred at the end of a  
336 decrease in global  $\delta^{13}\text{C}$ , suggesting that changes in the carbon cycle involving the terrestrial and  
337 deep-ocean carbon reservoirs were likely instrumental in driving late Miocene climate cooling.

338 The start of cooler climate conditions culminated with ephemeral Northern Hemisphere  
339 glaciations between 6.0–5.5 Ma (*ibid.*). From the above discussion, we conclude that although  
340 there are significant changes in global climate that occurred during the accumulation of the  
341 Nicobar Fan, none appear to uniquely bracket this time interval from ~9.5 Ma. This suggests  
342 another more local primary causal process.

343 The South Asian (Indian) monsoon would have had the most influence on fan sediment  
344 source areas, although the East Asian monsoon would have impacted the easternmost region  
345 including the syntaxis (Namche Barwa). The relationship between annual rainfall and its  
346 temporal distribution and erosion as a driver for increased sediment supply (Snyder *et al.*, 2003)  
347 implies that a stronger monsoon would generate increased physical erosion, fluvial transport and,  
348 therefore, lead to increased sediment accumulation rates in the submarine fans. At the present-  
349 day, the summer monsoon accounts for ~70% of annual rainfall in all catchments draining into  
350 the Bay of Bengal, but due to orographic forcing it focuses precipitation on the southern edge of  
351 the Lesser and Greater Himalayan Sequences of the Himalaya. The high- elevation, high- relief,  
352 and usually dry areas, are only affected by stronger monsoons and significant precipitation only  
353 occurs in the eastern syntaxial region during the winter season (Bookhagen and Burbank, 2010).

354 The intensity of the South Asian monsoon has been linked to the growth of the Himalaya,  
355 especially in the Miocene (Clift *et al.*, 2008), and the most significant changes in monsoon  
356 intensity took place in the middle Miocene, at ~12.9 Ma, when the monsoon wind system  
357 develop in strength and intensity similar to the present conditions (Betzler *et al.*, 2016). Proxy  
358 data indicate that from 11 Ma the summer monsoon was weak but had intensified across South  
359 and East Asia by 7 Ma (Wan *et al.*, 2007; Gupta *et al.*, 2015). However, when the summer  
360 monsoon was weaker the winter monsoon would have been stronger and Gupta *et al.* (2015)  
361 noted that higher sediment accumulation rates seen in the Himalayan foreland (Siwaliks) from  
362 11–7 Ma were probably linked to winter precipitation during strong Westerlies when summer  
363 monsoon winds were weaker. From ~7 Ma the long-term global cooling trend appears to have

364 coincided with intensification of the Asian winter monsoon recorded by a long-term trend toward  
365 heavier benthic  $\delta^{18}\text{O}$  maxima (Zachos *et al.*, 2001). The most intense maxima peaked between  
366 5.8–5.5 Ma before reversing in the Pliocene (Holbourn *et al.* 2018).

367 Stronger winter monsoons in the Miocene means that erosion would tend to be more  
368 concentrated on the upper slopes and the eastern syntaxial region, hence fan provenance should  
369 be biased towards these areas and that, over time, contributions from these sources should  
370 decrease as the summer monsoon strengthened. However, no obvious trend linked to monsoon  
371 changes is apparent within the two fan datasets. Bengal Fan thermochronological data (Najman *et*  
372 *al.*, 2019) record constant lag-times between ~12–5 Ma associated with steady erosion of the  
373 GHS and syntaxial antiform plus a significant component of the THS, but there is also a constant  
374 and significant presence of LHS material. The proportions of material from the various  
375 Himalayan units (i.e., GHS, THS and LHS) does not change until after 4 Ma, post peak summer  
376 monsoon strength at ~5.5 Ma. After this time there is a significant increase in zircons with ages <  
377 300 Ma, and thermochronometry data record short lag-times (Blum *et al.*, 2018; Najman *et al.*,  
378 2019) diagnostic of rapid exhumation of the eastern syntaxis (Najman *et al.*, 2019). Whilst  
379 inception of rapid syntaxial exhumation is considered to have started between 7–5 Ma (Bracciali  
380 *et al.*, 2016; Lang *et al.*, 2016), extremely rapid exhumation rates have only been sustained in the  
381 Namche Barwa Syntaxis region since 5 Ma (Lang *et al.*, 2016). At the present-day, the syntaxis  
382 region is noteworthy as a major source of sediment entering the Brahmaputra River system, as  
383 indicated by the sediment geochemistry, petrography, and thermochronology data from the  
384 Brahmaputra River and its tributaries that suggest 35–70% of the sediment flux of the  
385 Brahmaputra River were sourced in the Namche Barwa Syntaxis (Garzanti *et al.*, 2004; Singh  
386 and France-Lanord, 2002; Stewart *et al.*, 2008; Gemigani *et al.*, 2018). By contrast, Nicobar Fan  
387 samples record constant contributions from the GHS and THS, but LHS material is not always  
388 present. Further, in the Nicobar Fan no evidence such as zircon ages < 10 Ma, was found to

389 support significant input from the rapidly exhuming Namche Barwa massif of the eastern  
390 syntaxis.

391 Sediment accumulation in both fans reached their acme between ~9.5–8 Ma similar to  
392 major sedimentation in the Himalayan foreland that has been associated with a strong winter  
393 monsoon. It may be that climate has influenced MARS in both fan systems. However, post 9 Ma  
394 MARS vary between the two fans and changes in sediment provenance do not show a close  
395 correspondence to the increase in monsoon intensity that took place between 11–5 Ma or its  
396 subsequent weakening. This suggests differences in fan accumulation rates and provenance wss  
397 due to other primary causal processes.

398

## 399 4.2 Tectonics

400 From the above discussion, distinct changes in sediment accumulation that is common in  
401 both fans, occurred between 9.5–8.3 Ma (peak MARs) and 5.5–5.2 Ma (sharp drop in MARs).  
402 Similarly, both fans share a change in provenance between 5–3 Ma recorded by  
403 thermochronometry data that show a switch to rapid exhumation in the Bengal Fan source and a  
404 significant slow down in the Nicobar Fan sources (Fig. 8). This change coincided with low rates  
405 of accumulation in the Bengal Fan and a marked increase in the Nicobar Fan between 3.8–1.7  
406 Ma.

407 Perhaps the most important development was a change in the path of the paleo-  
408 Brahmaputra River, whereby prior to ~5 Ma the paleo-Brahmaputra River flowed directly south  
409 (Fig. 9; Najman *et al.* 2012; Govin *et al.* 2018) although from the late Miocene it would also have  
410 been pushed westwards by the expanding Indo–Burma wedge that also folded and exposed earlier  
411 sediments deposited in the foreland and remnant ocean basin including the Surma Basin (Najman  
412 *et al.* 2012; Betka *et al.*, 2018). The Indo–Burma wedge is a thin-skinned fold-thrust belt formed  
413 by oblique convergence and accretion of sediments of the Ganges–Brahmaputra Delta (GBD) on  
414 the Indian plate with the Shan Plateau (Betka *et al.*, 2018). The frontal fold-belt (Chittagong Hill

415 Tracts) records ongoing deformation of Paleogene – present Himalayan sourced fluvial-deltaic  
416 sedimentary rocks of the GBD (Najman *et al.*, 2012). These include the late Eocene to early  
417 Miocene Barail Formation and, in the outermost belt, the Miocene shallow-marine deposits of the  
418 Surma Group, overlain by Miocene–Pliocene Tipam Group fluvial deposits, and Pliocene–  
419 Quaternary Dupi Tila Group fluvial and alluvial deposits (Najman *et al.*, 2012). These have been  
420 folded into a series of fault-cored antiforms separated by wide and low-relief synclinal valleys  
421 and were sourced from the Himalaya with a minor arc-derived component from either the “Trans-  
422 Himalaya” or recycled from the arc-derived Paleogene Indo–Burman Ranges (Allen *et al.*, 2008;  
423 Najman *et al.*, 2012). Most of the deformation of this outer belt took place between 8–2 Ma based  
424 on zircon thermochronometry which limits deformation to < 8 Ma (Betka *et al.*, 2018) and onlaps  
425 across a latest Pliocene marker bed on a submarine anticline that dates deformation of the frontal  
426 part of the wedge to ~2 Ma (Maurin and Rangin, 2009).

427         The significance of the timing of the westward encroachment of the fold belt, which is  
428 also seen in seismic mapping across the Surma Basin (Najman *et al.*, 2012), is that it occurred at  
429 the same time as the uplift of the Shillong Plateau at 5.2–4.9 Ma (Govin *et al.*, 2018). This led to  
430 a diversion of the paleo-Brahmaputra River westwards around the Shillong Plateau producing an  
431 axial, east to west, route along strike of the mountain front before turning to drain southwards  
432 (Govin *et al.*, 2018). This development is constrained by fluvial deposits along the Dungsam Chu  
433 (Trans-Himalayan) foreland section of eastern Bhutan that show arrival of Trans-Himalayan  
434 (Cretaceous–Eocene zircon U–Pb ages) detritus from ~5 Ma onwards (Govin *et al.*, 2018).  
435 Although Brahmaputra River material now routed west of the Shillong Plateau, a southerly  
436 drainage also remained open to the east of the plateau until ~2 Ma when westward encroachment  
437 of the fold belt reached the margins of the Shillong Plateau. Evidence for this can be seen on  
438 seismic lines, and provenance of the Tipam Formation that was later recycled into the Dupi Tila  
439 Group (Najman *et al.*, 2012). Neogene deposits of the Surma Basin do not record evidence of the  
440 rise and erosion of the eastern syntaxis domal pop-up until the late Pliocene–Pleistocene

441 (Bracciali *et al.*, 2016) which is the time by which the southerly drainage east of the plateau had  
442 become closed. This explains why the Nicobar Fan samples do not contain zircon U–Pb ages  
443 diagnostic of the syntaxis region (ages <10 Ma), whereas the Bengal Fan samples do.

444 The onset of major river diversions at ~5 Ma coincided with a marked drop in MARS  
445 seen in both fans (Fig. 8). However, by 4 Ma accumulation rates in the Nicobar Fan increased  
446 again until ~2 Ma when there was another marked drop in accumulation rates that remained low  
447 thereafter. By contrast, the Bengal Fan accumulation rates remained low from ~5–0.5 Ma, after  
448 which there was a small increase. McNeill *et al.* (2017b) suggested the drop from ~2 Ma,  
449 supported the hypothesis that impingement of the NinetyEast Ridge on the Sunda Trench diverted  
450 the primary flux west of the ridge along with a concomitant rise in mid–late Pleistocene  
451 accumulation rates on the Bengal Fan (e.g., France-Lanord *et al.*, 2016). However, as discussed  
452 above, a westward re-routing of the Brahmaputra River may also have played a role leading up to  
453 final collision of the ridge with the subduction zone that blocked sediment supply from the north  
454 (Curry and Moore, 1974).

455 Whilst the MAR data and detrital zircon U–Pb data suggest changes related to re-  
456 organisation of river routing to the fans, the detrital AFT show a constant behaviour in terms of  
457 apatite sources until 2 Ma, after which the data suggest a modest slowdown. The main age trend  
458 seen in the lag-time plot of figure 7 reflects a constant supply from a source area undergoing  
459 steady erosion through time. The short lag-time rules out significant intermediate storage and  
460 mixing. The source of apatites is indicated by unreset Siwalik foreland sediments in the  
461 Arunachal Pradesh, eastern Bhutan, and Nepal. Here, sands of comparable deposition ages to  
462 Nicobar Fan samples yielded identical AFT ages (Table 1) and lag times (Fig. 7). In the  
463 Arunachal Pradesh sands, with depositional ages between 0–2 Ma, the dominant population of  
464 AFT ages range from  $2.9 \pm 0.8$  Ma to  $4.0 \pm 0.9$  Ma with a secondary population between 7–15 Ma  
465 (Chirouze *et al.*, 2013). Similar ages are seen to the west in the foreland of Eastern Bhutan. Here,  
466 most dominant populations of unreset apatites record AFT ages between from  $3.6 \pm 0.8$  Ma

467 (youngest) up to  $6.9 \pm 1.2$  Ma (8 Ma sample) and secondary populations from 15–10 Ma (Coutand  
468 *et al.*, 2016). By contrast, modern bedrock AFT ages from the Shillong Plateau are older, ranging  
469 from 12.6–8.6 Ma and up to 101 Ma (Biswas, 2007), which rules out this block as a major  
470 sediment source for Nicobar Fan apatites.

471

### 472 4.3 Implications for sediment supply

473 The Nicobar Fan and Bengal Fan can be considered as the respective eastern and western  
474 parts of an integrated submarine-fan system. Their constituent sediments have the same  
475 provenance, whether delivered by the eastern or western routes from the Brahmaputra River. At  
476  $\sim 2$  Ma, the eastern drainage route to the Nicobar Fan became closed to direct input from the  
477 Ganges-Brahmaputra system, at which time the MARS in Nicobar Fan significantly decreased.

478 The earliest onset of high MARs in the Bengal Fan occurred at  $\sim 14$ – $13.5$  Ma, with a  
479 switch to the Nicobar Fan at  $\sim 9.5$  Ma (Fig. 9). The earliest high MARs in the Bengal Fan are  
480 broadly consistent with the observed rapid increase in seawater  $^{187}\text{Os}/^{188}\text{Os}$  and decrease in  
481 seawater  $^{87}\text{Sr}/^{86}\text{Sr}$  in the mid to late Miocene at  $\sim 16$ – $11$  Ma, which we interpret to reflect rapid  
482 thrust belt advance and exhumation of the outer Lesser Himalaya (Colleps *et al.*, 2018). The  
483 earliest high MARs in the Nicobar Fan do not demand a similar tectonic explanation in the  
484 Himalaya and other associated northern source areas for sediment supply via the Ganges–  
485 Brahmaputra drainage basin. The MARs most likely reflect an autocyclic shift from the  
486 importance of sediment routing in submarine channel systems to the west of the NinetyEast  
487 Ridge (Bengal Fan) to an eastern predominance (Nicobar Fan), i.e., switching to a dominance of  
488 fan deposition on the Nicobar Fan. However, an inspection of the MARs for the both the Bengal  
489 and Nicobar fans shows that the high MARs in the Bengal Fan do not show a substantial decrease  
490 until  $\sim 8.5$ – $8$  Ma, at least 1 Myr after the dramatic increase in the Nicobar Fan (Fig. 9), suggesting  
491 that other contributory factors, (e.g., tectonic), maintained the overall high sediment flux. For  
492 example, a comprehensive magnetostratigraphic and sedimentologic study of the Dati Basin in

493 the northern Himalaya Mountains by Zhang *et al.* (2019) recorded pulses of accelerated tectonic  
494 uplift and erosion of the Himalaya Mountains at ~10.0 Ma, ~3.0 Ma, and at ~1.7 Ma.

495 At ~5 Ma, a drop in MARs is observed in both the Nicobar Fan and Bengal fans. Also, at  
496 ~5 Ma, there was a change in river drainage to west of uplifting Shillong Plateau, but as seen in  
497 the provenance (Tipam Formation; Shrivastava *et al.*, 1974; Sahoo and Gogoi, 2009; Sarma and  
498 Chutia, 2013). Drainage remained open to the east of the Shillong Plateau.

499 At ~4–3.5 Ma, an increase in MARs is recorded in the Nicobar Fan, but the Bengal Fan  
500 MARs remained low. These younger increased MARs might be related to accelerated erosion in  
501 the Namche Barwa syntaxis with hysteresis effects. The inception of rapid syntaxial exhumation  
502 started between 7–5 Ma (Bracciali *et al.*, 2016) and extremely rapid exhumation rates have been  
503 sustained in the Namche Barwa region since ~5 Ma (Lang *et al.*, 2016). The syntaxis region is  
504 noteworthy as a major source of sediment entering the Brahmaputra based on studies using  
505 sediment geochemistry, petrography, and thermochronology data from the Brahmaputra and its  
506 tributaries that estimate 35–70% of the sediment flux of the Brahmaputra was sourced Namche  
507 Barwa (Enkelmann *et al.*, 2011; Garzanti *et al.*, 2004; Gemigani *et al.*, 2018; Singh and France-  
508 Lanord, 2002; Stewart *et al.*, 2008). Note that the Neogene Surma Basin does not record evidence  
509 of the rise and erosion of the domal pop-up until latest Pliocene–Pleistocene time (Bracciali *et al.*,  
510 2016) and that Nicobar Fan samples do not contain zircon U–Pb ages diagnostic of this region  
511 (ages < 10 Ma), whereas Bengal Fan samples do.

512 Since ~10 Ma, global sea level has generally fallen (Miller *et al.*, 2005), thereby  
513 decreasing accommodation on the shelf, and thus amplifying the processes driving sediment  
514 southward into the deep Indian Ocean. A fundamental question, however, is the reason for the  
515 submarine routing system to favour the Nicobar Fan over the Bengal Fan since ~9.5–2 Ma.

516

517 5. Conclusions

518 U–Pb age spectra of detrital zircons, sand petrography, and heavy-mineral analysis  
519 confirm that the Nicobar Fan was a major sink for Himalaya-derived material. Our data show the  
520 Nicobar Fan sands are similar but not identical to Bengal Fan sands, such that the Nicobar Fan  
521 sands lack young zircons derived from the eastern Himalayan syntaxis. These are present in  
522 Bengal Fan sands deposited after < 3 Ma. This timing coincides with the group of Bengal Fan  
523 samples that show closest affinity to the Brahmaputra River that re-routed at that time to a  
524 modern configuration. The Nicobar Fan samples show AFT ages consistent with erosion of the  
525 frontal Himalaya and/or contemporaneous erosion of similar age foreland sediments.

526 The petrographic data suggests that supply from the metamorphic axial core of the  
527 Himalayan range (GHS) has increased in the last 5.5 Ma. The down-core decrease in heavy-  
528 mineral concentration and the proportion of transparent heavy minerals relative to the heavy  
529 fraction also may be effects of intrastratal solution and grain size. The coarsening-upward trend  
530 indicated by the samples explains the upward decrease in the epidote/garnet ratio.

531 Apatite fission track data shows that source area exhumation, routing and burial were  
532 extremely rapid from ~8–3 Ma. This broadly corresponds to a time of fan re-organisation. We  
533 interpret this latter signal as due to both rapid rapid exhumation in the source area and lowered  
534 mean sea level during global cooling. The more distant Investigator Fan and the thick  
535 accretionary prism of the Sunda subduction zone of the easternmost Indian Ocean also contain  
536 significant amounts of Oligocene-Miocene Himalaya-derived material.

537 We conclude that although there are significant changes in global climate that occurred  
538 during the accumulation of the Nicobar Fan, none appear to uniquely bracket the time interval  
539 from ~9.5 Ma when high and sustained MARs began. Similar arguments can be made for the  
540 Bengal Fan. Since ~5 Ma, tectonically driven changes in the river network most influenced fan  
541 sedimentation and provenance. These changes can account for the main differences seen between  
542 the Bengal and Nicobar Fan, that were enhanced by the global deterioration in climate and  
543 associated eustatic sea-level falls, to strengthen the sediment flux to the Nicobar and Bengal fans.

544

545 References

546

547 Allen, R., Najman, Y., Carter, A., Barfod, D., Bickle, M.J., Chapman, H.J., Garzanti, E., Vezzoli,  
548 G., Andò, S. and Parrish, R. 2008. Provenance of the Tertiary sedimentary rocks of the Indo-  
549 Burman Ranges, Burma (Myanmar): Burman arc or Himalayan-derived? *Journal of the*  
550 *Geological Society London*, 165, 1045–1057.

551

552 Andò, S., Garzanti, E., Padoan, M. and Limonta, M. 2012. Corrosion of heavy minerals during  
553 weathering and diagenesis: a catalog for optical analysis. *Sedimentary Geology*, 280, 165-178.

554

555 Betka, P.M., Seeber, L., Thomson, S.N., Steckler, M.S., Sincavage, R. and Zoramthara, C. 2018.  
556 Slip-partitioning above a shallow, weak décollement beneath the Indo-Burman accretionary  
557 prism. *Earth and Planetary Science Letters*, 503, 17–28.

558

559 Betzler, C. *et al.* 2016. The abrupt onset of the modern South Asian Monsoon winds. *Science*  
560 *Report*, 6, 29838; doi: 10.1038/srep29838.

561

562 Biswas, S., Coutand, I., Grujic, D., Hager, C., Stockli, D. and Grasemann, B., 2007. Exhumation  
563 and uplift of the Shillong Plateau and its influence on the eastern Himalayas: new constraints  
564 from apatite and zircon (U–Th–[Sm])/He and apatite fission track analyses. *Tectonics*, 26,  
565 TC6013.

566

567 Bracciali, L., Parrish, R.R., Najman, Y., Smye, A.J., Carter, A. and Wijbrans, J.R. 2016. Plio-  
568 Pleistocene exhumation of the eastern Himalayan syntaxis and its domal 'pop-up'. *Earth Science*  
569 *Reviews*, 160, 350–385.

570

571 Blum, M., Kimberly Rogers, K., Gleason, J., Najman, Y., Cruz, J. and Fox, L. 2018. Allogenic  
572 and autogenic signals in the stratigraphic record of the deep-sea Bengal Fan. *Nature Scientific*  
573 *Reports*, 8, 7973. doi:10.1038/s41598-018-25819-5.

574

575 Bookhagen, B. and Burbank, D.W. 2010. Toward a complete Himalayan hydrological budget:  
576 Spatiotemporal distribution of snowmelt and rainfall and their impact on river discharge. *Journal*  
577 *of Geophysical Research*, 115, F03019, doi:10.1029/2009JF001426

578

579 Booth, A.L., Zeitler, P.K., Kidd, W.S., Wooden, J., Liu, Y., Idleman, B., Hren, M. and  
580 Chamberlain, C.P. 2004. U-Pb Zircon constraints on the tectonic evolution of southeastern Tibet,  
581 Namche Barwa area. *American Journal of Science*, 304, 889–929.

582

583 Campbell, I.H., Reiners, P.W., Allen, C.M., Nicolescu, S. and Upadhyay, R. 2005. He–Pb double  
584 dating of detrital zircons from the Ganges and Indus Rivers: Implication for quantifying sediment  
585 recycling and provenance studies. *Earth and Planetary Science Letters*, 237, 402–432.

586

587 Chirouze, F., Huyghe, P., van der Beek, P., Chauvel, C., Chakraborty, T., Dupont-Nivet, G. and  
588 Bernet, M. 2013. Tectonics, exhumation, and drainage evolution of the eastern Himalaya since 13  
589 Ma from detrital geochemistry and thermochronology, Kameng River, Section, Arunachal  
590 Pradesh. *Geological Society of America Bulletin*, 125, 523–538.

591

592 Clift, P.D., Hodges, K.V., Heslop, D., Hannigan, R., van Long, H. and Calves, G. 2008.  
593 Correlation of Himalayan exhumation rates and Asian monsoon intensity. *Nature Geoscience*, 1,  
594 875–880.

595

596 Colleps, C.L., Ryan McKenzie, N., Stockli, D.F., Hughes, N.C., Singh, B.P., Webb, A.A.G.,  
597 Myrow, P.M., Planavsky, N.J. and Horton, B.K. 2018. Zircon (U-Th)/He Thermochronometric  
598 constraints on Himalayan thrust belt exhumation, bedrock weathering, and Cenozoic seawater  
599 chemistry. *Geochemistry, Geophysics, Geosystems*, 19, 257–271.

600

601 Coutand, I., Barrier, L., Govin, G., Grujic, D., Hoorn, C., Dupont-Nivet, G. and Najman, Y.  
602 2016. Late Miocene-Pleistocene evolution of India-Eurasia convergence partitioning between the  
603 Bhutan Himalaya and the Shillong Plateau: New evidences from foreland basin deposits along  
604 the Dungsam Chu section, eastern Bhutan. *Tectonics*, 35, 2963–2994.

605

606 Curray, J.R. 1991. Possible greenschist metamorphism at the base of a 22-km sedimentary  
607 section, Bay of Bengal. *Geology*, 19, 1097–1100.

608

609 Curray, J.R. and Moore, D.G. 1971. Growth of the Bengal deep-sea fan and denudation in the  
610 Himalayas. *Geological Society American Bulletin*, 82, 563–572.

611

612 DeCelles, P.G., Gehrels, G.E., Quade, J., Ojha, T.P., Kapp, P.A. and Upreti, B.N. 1998. Neogene  
613 foreland basin deposits, erosional unroofing, and the kinematic history of the Himalayan fold-  
614 thrust belt, western Nepal. *Geological Society of America Bulletin*, 110, 2-21.

615

616 France-Lanord, C., Spiess, V., Klaus, A. and the Expedition 354 Scientists 2016. *Neogene and*  
617 *late Paleogene record of Himalayan orogeny and climate: a transect across the Middle Bengal*  
618 *Fan. International Ocean Discovery Program Expedition, 354*, Preliminary Report, Bengal Fan.

619

620 Galbraith, R.F. 2005. Statistics for Fission Track Analysis. Interdisciplinary Statistics Series, 224  
621 pp. Chapman and Hall/CRC.

622

623 Garzanti, E. 2016. From static to dynamic provenance analysis - sedimentary petrology upgraded.  
624 *Sedimentary Geology*, 336, 3–13.

625

626 Garzanti, E., Vezzoli, G., Andò, S., France-Lanord, C., Singh, S.K. and Foster, G. 2004. Sand  
627 petrology and focused erosion in collision orogens: the Brahmaputra case. *Earth and Planetary  
628 Science Letters*, 220, 157–174.

629

630 Garzanti, E., Andó, S., France-Lanord, C., Vezzoli, G. and Najman, Y. 2010. Mineralogical and  
631 chemical variability of fluvial sediments. 1. Bedload sand (Ganga-Brahmaputra, Bangladesh).  
632 *Earth and Planetary Science Letters*, 299, 368–381.

633

634 Garzanti, E. 2019. The Himalayan Foreland Basin from collision onset to the present: a  
635 sedimentary–petrology perspective. *In*: Treloar, P.J. and Searle, M.P. (eds), *Himalayan  
636 Tectonics: A Modern Synthesis*. Geological Society, London, Special Publications, 483, 65–122.

637

638 Geersen, J., Bull, J.M., McNeill, L.C., Henstock, T.J., Gaedicke, C., Chamot-Rooke, N. and  
639 Delescluse, M. 2015. Pervasive deformation of an oceanic plate and relationship to large >MW8  
640 intraplate earthquakes: The northern Wharton Basin, Indian Ocean. *Geology*, 43, 359–362.

641

642 Gehrels, G., Kapp, P., DeCelles, P., Pullen, A., Blakey, R., Weislogel, A., Ding, L., Guynn, J.,  
643 Martin, A., McQuarrie, N. and Yin, A. 2011. Detrital zircon geochronology of pre-Tertiary strata  
644 in the Tibetan-Himalayan orogen. *Tectonics*, 30, 1944–1994.

645

646 Gemignani, L., van der Beek, P.A. Braun, J., Najman, Y., Bernet, M., Garzanti, E. and Wijbrans,  
647 J.R. 2018. Downstream evolution of the thermochronologic age signal in the Brahmaputra

648 catchment (eastern Himalaya): Implications for the detrital record of erosion. *Earth and*  
649 *Planetary Science Letters*, 499, 48–61.

650

651 Govin, G., Najman, Y., Dupont-Nivet, G., Millar, I., van der Beek, P., Huyghe, P., O'Sullivan, P.,  
652 Mark, C. and Vögell, N. 2018. The tectonics and paleo-drainage of the easternmost Himalaya  
653 (Arunachal Pradesh, India) recorded in the Siwalik rocks of the foreland basin. *American Journal*  
654 *of Science*, 318, 764–798.

655

656 Gupta, K., Yuvaraja, A., Prakasam, M., Clemens, S. C. and Velu, A. 2015. Evolution of the  
657 South Asian monsoon wind system since the late Middle Miocene. *Palaeogeography*,  
658 *Palaeoclimatology. Palaeoecology*. 438, 160–167.

659

660 Heroy, D.C., Kuehl, S.A. and Goodbred, S.L. 2003. Mineralogy of the Ganges and Brahmaputra  
661 Rivers: implications for river switching and Late Quaternary climate change. *Sedimentary*  
662 *Geology*, 155, 343–359.

663

664 Holbourn, A., Kuhnt, W., Clemens, S., Prell, W. and Andersen, N. 2013. Middle to late Miocene  
665 stepwise climate cooling: evidence from a high-resolution deep water isotope curve spanning 8  
666 million years. *Paleoceanography*, 28, 688–699.

667

668 Holbourn, A.E., Kuhnt, W., Clemens, S.C., Kochmann, K.G.D., Jöhnck, J., Lubbers, J. and  
669 Andersen, N. 2018. Late Miocene climate cooling and intensification of southeast Asian winter  
670 monsoon. *Nature Communications*, doi: 10.1038/s41467-018-03950-1.

671

672 Ingersoll, R.V. and Suczek, C.A. 1979. Petrology and provenance of Neogene sand from Nicobar  
673 and Bangal fans, Deep Sea Drilling Project Sites 211 and 218. *Journal of Sedimentary Petrology*,  
674 49, 1217–1228.

675

676 Jena B., Kurian, P.J. and Avinash, K. 2016. Morphology of submarine channel-levee systems in  
677 the eastern Bay of Bengal near Andaman region. *Journal of Coastal Conservation*, 20, 211–220.

678

679 Ji, W-Q., Wu, F-Y., Liu, X-C., Liu, Z-C., Zhang, C., Liu, T., Wang, J-G. and Paterson, S.R.  
680 2019. Pervasive Miocene melting of thickened crust from the Lhasa terrane to Himalaya,  
681 southern Tibet and its constraint on generation of Himalayan leucogranite. *Geochimica et*

682 *Cosmochimica Acta*, doi.org/10.1016/j.gca.2019.07.048

683

684 Lang, K.A., Huntington, K.W., Burmester, R. and Housen, B. 2016. Rapid exhumation of the  
685 eastern Himalayan syntaxis since the late Miocene. *Geological Society of America Bulletin*, 128,  
686 1403–1422. Doi:10.1130/B31419

687

688 Limonta, M., Resentini, A., Carter, A., Bandopadhyay, P.C. and Garzanti, E. 2017. Provenance  
689 of Oligocene Andaman sandstones (Andaman–Nicobar Islands): Ganga–Brahmaputra or

690 Irrawaddy derived? *In*: Bandopadhyay, P.C. and Carter, A. (eds), *The Andaman–Nicobar*

691 *Accretionary Ridge: Geology, Tectonics and Hazards*, 143–154. Geological Society London

692 Memoir, 47.

693

694 Lyle, M., Barron, J., Bralower, T.J., Huber, M., Lyle, A.O., Ravelo, A.C., Rea, D.K. and Wilson,  
695 P.A. 2008. Pacific Ocean and Cenozoic evolution of climate. *Reviews in Geophysics*, 46,

696 RG2002, doi:10.1029/2005RG000190.

697

698 Maurin, T. and Rangin, C. 2009. Structure and kinematics of the Indo-Burmese Wedge: Recent  
699 and fast growth of the outer wedge. *Tectonics*, 28, TC2010, doi:10.1029/  
700

701 McNeill, L.C., Dugan, B., Petronotis, K.E., Backman, J., Bourlange, S., Chemale, F., Chen, W.,  
702 Colson, T.A., Frederik, M.C.G., Guèrin, G., Hamahashi, M., Henstock, T., House, B.M., Hüpers,  
703 A., Jeppson, T.N., Kachovich, S., Kenigsberg, A.R., Kuranaga, M., Kutterolf, S., Milliken, K.L.,  
704 Mitchison, F.L., Mukoyoshi, H., Nair, N., Owari, S., Pickering, K.T., Pouderoux, H.F.A., Yehua,  
705 S., Song, I., Torres, M.E., Vannucchi, P., Vrolijk, P.J., Yang, T. and Zhao, X. 2017a. Expedition  
706 362 methods. *In*: McNeill, L.C., Dugan, B., Petronotis, K.E., and the Expedition 362 Scientists,  
707 *Sumatra Subduction Zone. Proceedings of the International Ocean Discovery Program*, 362,  
708 Sumatra Subduction Zone. College Station, TX (International Ocean Discovery Program).  
709 <https://doi.org/10.14379/iodp.proc.362.102.2017>  
710

711 McNeill, L.C., Dugan, B., Backman, J., Pickering, K.T., Pouderoux, H.F.A., Henstock, T.J.,  
712 Petronotis, K.E., Carter, A., Chemale, F. Jr., Milliken, K.L., Kutterolf, S., Mukoyoshi, H.,  
713 Chen, W., Kachovich, S., Mitchison, F.L., Bourlange, S., Colson, T.A., Frederik, M.C.G., Gilles  
714 Guèrin, G., Hamahashi, M., House, B.M., Hüpers, A., Jeppson, T.N., Kenigsberg, A.R.,  
715 Kuranaga, M., Nair, N., Owari, S., Shan, Y., Song, I., Torres, M.E., Paola Vannucchi, P., Vrolijk,  
716 P.J., Yang, T., Xixi Zhao, X. and Thomas, E. 2017b. Understanding Himalayan erosion and the  
717 significance of the Nicobar Fan. *Earth and Planetary Science Letters*, 475, 134–142.  
718 doi:10.1016/j.epsl.2017.07.019  
719

720 Miller, K.G, Kominz, M.A., Browning, J.V., Wright, J.D., Mountain, G.S. and Katz, M.E. 2005.  
721 The Phanerozoic record of global sea-level change. *Science*, 310, 1293–1298.  
722

723 Mitchell, A., Chung, S.L., Oo, T., Lin, T.H. and Hung, C.H. 2012. Zircon U–Pb ages in

724 Myanmar: Magmatic–metamorphic events and the closure of a neo–Tethys ocean. *Journal of*  
725 *Asian Earth Sciences*, 56, 1–23.

726

727 Najman, Y. and Garzanti, E. 2000. Reconstructing early Himalayan tectonics evolution and  
728 paleogeography from Tertiary foreland basin sedimentary rocks, northern India.  
729 *Geological Society of America Bulletin*, 112, 435–449.

730

731 Najman, Y., Bickle, M, BouDagher-Fadel, M., Carter, A., Garzanti, E., Paul, M., Wijbrans, J.,  
732 Willett, E., Oliver, G., Parrish, R., Akhter, H., Allen, R., Ando, S., Chisty, E., Reisberg, L. and  
733 Vezzoli, G. 2008. The Paleogene record of Himalayan erosion: Bengal Basin, Bangladesh. *Earth*  
734 *and Planetary Science Letters*, 273,1–14.

735

736 Najman, Y., Allen, R., Willett, E, Carter, A, Barford, D., Garzanti, E, Wijbrans, J., Bickle, M.,  
737 Vezzoli, G., Ando, S., Oliver, G and Uddin, M.J. 2012, 'The record of Himalayan erosion  
738 preserved in the sedimentary rocks of the Hatia Trough of the Bengal Basin and the Chittagong  
739 Hill Tracts, Bangladesh'. *Basin Research*, 24, 499– 519.

740

741 Najman, Y., Mark, C., Barfod, D.N., Carter, A., Parrish, R., Chew, D. and Gemignani, L. 2019.  
742 Spatial and temporal trends in exhumation of the Eastern Himalaya and syntaxis as determined  
743 from a multitechnique detrital thermochronological study of the Bengal Fan. *Geological Society*  
744 *of America Bulletin*, 131, 1607–1622.

745

746 Pickering, K.T. and Hiscott, R.N. (with contribution by Heard, T.G.) 2016. *Deep Marine*  
747 *Systems: Processes, Deposits, Environments, Tectonic and Sedimentation*. Wiley and American  
748 Geophysical Union (AGU), 672 pp. ISBN: 978-1-4051-2578-9.

749

750 Pickering, K.T., Pouderoux, H., McNeill, L.C., Backman, J., Chemale, F., Kutterolf, S., Milliken,  
751 K., Mukoyoshi, H., Henstock, T.J., Stevens, D.E., Parnell, C. and Dugan, B. 2019.  
752 Sedimentology, stratigraphy and architecture of the Nicobar Fan (Bengal–Nicobar Fan System),  
753 Indian Ocean: Results from International Ocean Discovery Program Expedition 362.  
754 *Sedimentology*, doi: 10.1111/sed.12701.  
755  
756 Robinson, R.A.J., Brezina, C.A., Parrish, R.R., Horstwood, M.S.A., Oo, N.W., Bird, M.I.,  
757 Thein, M., Walters, A.S., Oliver, G.J.H. and Zaw, K. 2014. Large rivers and Orogens: the  
758 evolution of the Yarlung Tsangpo–Irrawaddy system and the eastern Himalayan syntaxis.  
759 *Gondwana Research*, 26, 112–121.  
760  
761 Sahoo, M. and Gogoi, K.D. 2009. Depositional history, processes and mechanism of early  
762 Miocene sediments of Upper Assam Basin. *Journal of the Geological Society of India*, 73, 575–  
763 585.  
764  
765 Sarma, J.N. and Chutia, A. 2013. Petrography of sub-surface Tipam Sandstone Formation of a  
766 part of Upper Assam Basin, India. *Global Research Analysis*, 2, 112–113.  
767  
768 Shrivastava, P.K., Ganeshan, S. and Ray, D. 1974. Tipam Group in the Subsurface of Upper  
769 Assam Valley, South of Brahmaputra. *Journal of the Geological Society of India*, 15, 165–181.  
770  
771 Singh, S.K., France-Lanord, C. 2002. Tracing the distribution of erosion in the Brahmaputra  
772 watershed from isotopic compositions of stream sediments. *Earth and Planetary Science Letters*,  
773 202, 645–662.  
774

775 Snyder, N.P., Whipple, K.X., Tucker, G.E. and Merritts, D.J. 2003. Importance of a stochastic  
776 distribution of floods and erosion thresholds in the bedrock river incision problem, *Journal*  
777 *Geophysical Research*, 108(B2), 2117, doi:10.1029/2001JB001655

778

779 Stewart, R.J., Hallet, B., Zeitler, P.K., Malloy, M.A., Allen, C.M. and Trippett, D. 2008.  
780 Brahmaputra sediment flux dominated by highly localized rapid erosion from the easternmost  
781 Himalaya. *Geology*, 36, 711–739.

782

783 Thiede, R.C. and Ehlers, T.A. 2013. Large spatial and temporal variations in Himalayan  
784 denudation. *Earth and Planetary Science Letters*, 371, 278–293.

785

786 Thompson, R.W. 1974. Mineralogy of sands from the Bengal and Nicobar fans, sites 218 and  
787 211, eastern Indian Ocean. *In*: von der Borch, C.C., Sclater, J.G. *et al.* (eds), Initial Reports of the  
788 Deep Sea Drilling Project, 22, 711–713. United States Government Printing Office, Washington,  
789 DC.

790

791 Vermeesch, P. 2012. On the visualisation of detrital age distributions. *Chemical Geology*, 312-  
792 313, 190–194, doi: 10.1016/j.chemgeo.2012.04.021.

793

794 Vermeesch, P. 2013, Multi-sample comparison of detrital age distributions. *Chemical Geology*,  
795 341, 140– 146.

796

797 Wan, S., Li, A., Clift, P.D. and Stuut, J-B.W. 2007. Development of the East Asian monsoon:  
798 mineralogical and sedimentologic records in the northern South China Sea since 20 Ma.  
799 *Palaeogeography, Palaeoclimatology, Palaeoecology*, 254, 561–582.

800

801 Yokohama, K., Amano, K., Taira, A. and Saito, Y. 1990. Mineralogy of silts from the Bengal  
802 Fan. *In*: Cochran, J.R., Stow, D.A.V. *et al.* (eds) Proceedings of the Ocean Drilling Program,  
803 Scientific Results, 116, 59–73. Ocean Drilling Program, College Station, Texas.

804

805 Zachos, J.C., Pagani, M., Sloan, L., Thomas, E and Billups, K. 2001. Trends, rhythms, and  
806 aberrations in global climate 65 Ma to present. *Science*, 292, 689–693.

807

808 Zhang, W., Zhang, D., Fang, X., Zhang, T., Chen, C. and Yan, M. 2019. New paleomagnetic  
809 constraints on rift basin evolution in the northern Himalaya mountains. *Gondwana Research*, 77,  
810 98–110.

811

## 812 List of figures

813 Figure 1. Regional map of the Bengal Nicobar and Investigator fans. The map includes the deep-  
814 marine sedimentary system with fans separated by ridges, the Ganges–Brahmaputra River  
815 system, and relevant DSDP/ODP/IODP drill sites. No identifiable Bengal Fan sediments were  
816 found at DSDP Site 213, and DSDP Site 215 shows a hiatus from lower Eocene clay and  
817 nanofossil ooze to lower Miocene silty clay, that Curray (1991) interpreted as distal Bengal Fan  
818 sediments. DSDP Site 211 has a hiatus from non-fossiliferous clays overlying Maastrichtian to  
819 Pliocene strata, again probably distal fan sediments. The Investigator Fan, where Site 211 is  
820 located, is called after the Investigator Ridge. Channels recognised on the seafloor are reported  
821 after Curray and Moore (1971). Top right inset is a bathymetry map of the seafloor around IODP  
822 Expedition 362 sites (modified from Geersen *et al.*, 2015); note the presence of well-identified  
823 channel heading south. The black box at ~10°N shows the study area of Jena *et al.* (2016) who  
824 proved the connection between channel E7 in the Bengal Fan and the Nicobar Channel.

825 Figure 2. Geology of potential source areas for the sediments in the Nicobar and Bengal  
826 submarine fans. Modified after Mitchell *et al.* (2012) and Robinson *et al.* (2014).

827 Figure 3. Schematic summary of lithostratigraphic units and subunits defined during IODP  
828 Expedition 362 in Holes U1480E–U1480G. Drilling in the nearby Hole U1481 recovered core  
829 from Units II and III. Sand-prone intervals were defined from a synthesis of the sand-size fraction  
830 in recovered cores. Modified from McNeill *et al.* (2017a).

831 Figure 4. QFL diagram showing the progressive upward change of detrital modes, from  
832 feldspatho-litho-quartzose Petrofacies D (grey) and litho-feldspatho-quartzose Petrofacies C  
833 (yellow), to quart-rich feldspatho-quartzose Petrofacies B (orange), and eventually feldspatho-  
834 quartzose Petrofacies A (red). In Petrofacies D, the grey colour of the symbols becomes darker  
835 with depth; conversely, colours become brighter up-section in symbols of other petrofacies.  
836 Classification fields are after Garzanti (2016).

837 Figure 5. Sample detrital zircon U–Pb age distributions plotted as adaptive kernel density  
838 estimates (Vermeesch, 2013), comparing data from this study with Bengal Fan dataset of Blum *et*  
839 *al.* (2018) and representative river sands from the Ganges and Brahmaputra rivers.

840 Figure 6. (A) Multidimensional scaling maps (MDS) comparing zircon U–Pb datasets for the  
841 Nicobar and Bengal fans, Ganges and Brahmaputra rivers (data from Blum *et al.*, 2018). Pink  
842 circles show BF, brown Nicobar Fan and blue river samples. Numbers refer to sample age (Ma).  
843 Note the branch of Bengal Fan samples that most closely resemble the modern Brahmaputra are  
844 all  $\leq 3.2$  Ma. (B) Differences between the Nicobar and Bengal fans highlighted by the red circled  
845 area on the MDS plot in 6A is largely due to a higher percentage of young ( $< 50$  Ma) grain ages  
846 for samples with a deposition age  $< 4$  Ma in the BF samples. (C) MDS map comparing fan  
847 samples with stratigraphic units of the Surma Basin (yellow) and Pliocene Himalayan foreland  
848 sediments (green) from the Dungsam Chu section eastern Bhutan (Govin *et al.*, 2018). (D)  
849 Compares the percentage contributions using the age groups of Blum *et al.* (2018).

850 Figure 7. Graph showing lag-time relationships between sample depositional age and youngest  
851 population of apatite fission track ages for samples from the Nicobar Fan and unreset Siwalik  
852 foreland sediments.

853 Figure 8. Mass accumulation rates (MARs) for IODP sites 1451 (Bengal Fan) and 1480 (Nicobar  
854 Fan) from Pickering *et al.* (2019).

855 Figure 9. Links between submarine-fan MARS and paleogeographic and drainage changes since  
856 the late Miocene. Fan reconstructions after McNeill *et al.* (2017) and upper three maps show  
857 major river drainage changes adapted from Govin *et al.* (2018), and Najman *et al.* (2012). Arrows  
858 link paleogeographic maps with relevant parts of the MAR graph for both the Nicobar and  
859 Bengal fans. IBR = Indo-Burman Range; SB = Surma Basin; DC = Dungsam Chu section; NP =  
860 Namcha Barwa.

861

## 862 List of tables

863 Table 1: Summary of AFT results. Samples of similar deposition age shown in italics were  
864 combined for age component modelling. Included for comparison are the main provenance ages  
865 of unreset Siwalik foreland sediments of comparable deposition age (Chirouz *et al.*, 2013;  
866 Coutand *et al.*, 2016). Errors on ages are 1sigma.

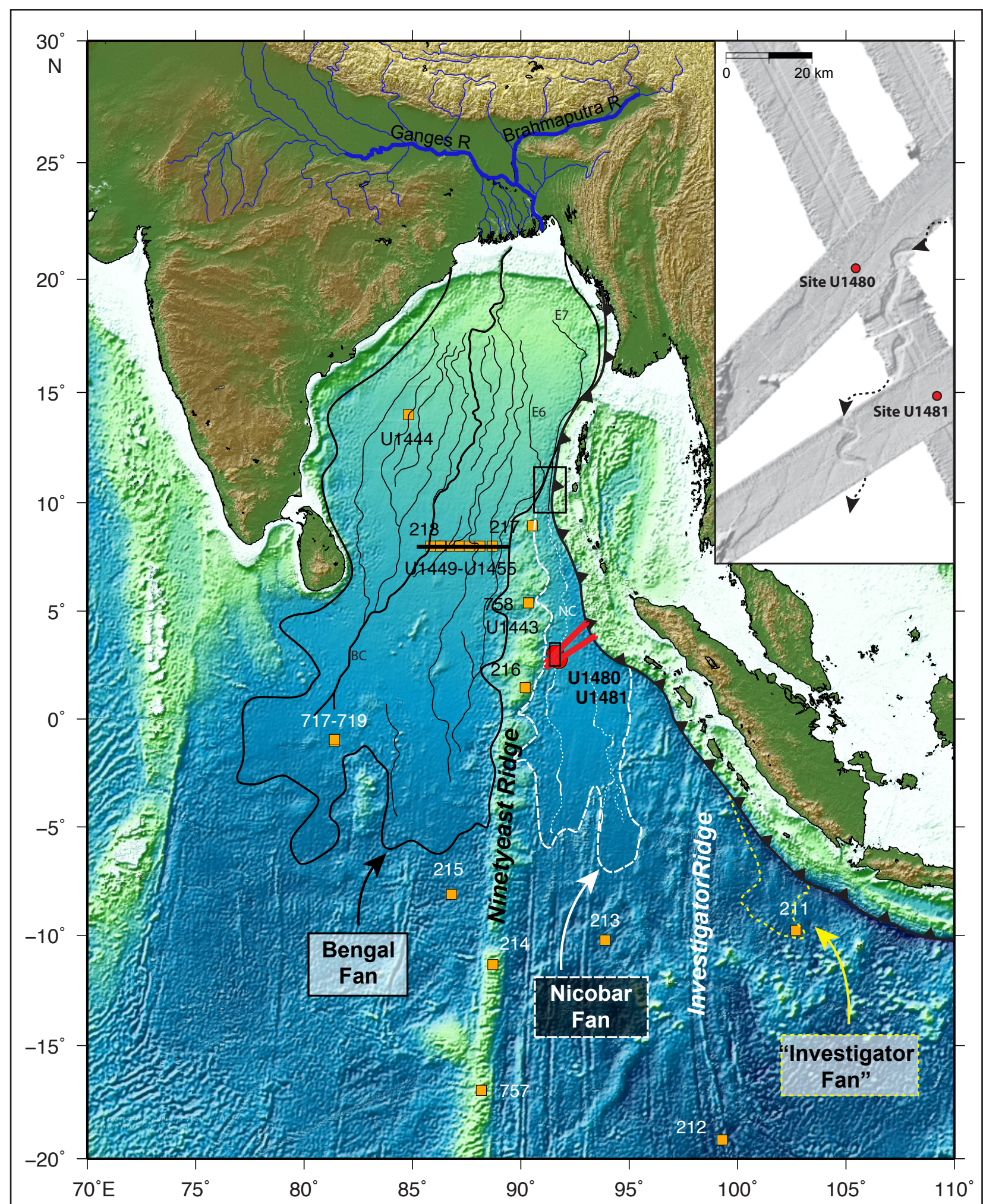


**Figure 2**  
[Click here to download Figure: Fig2\\_Pickering et al.pdf](#)

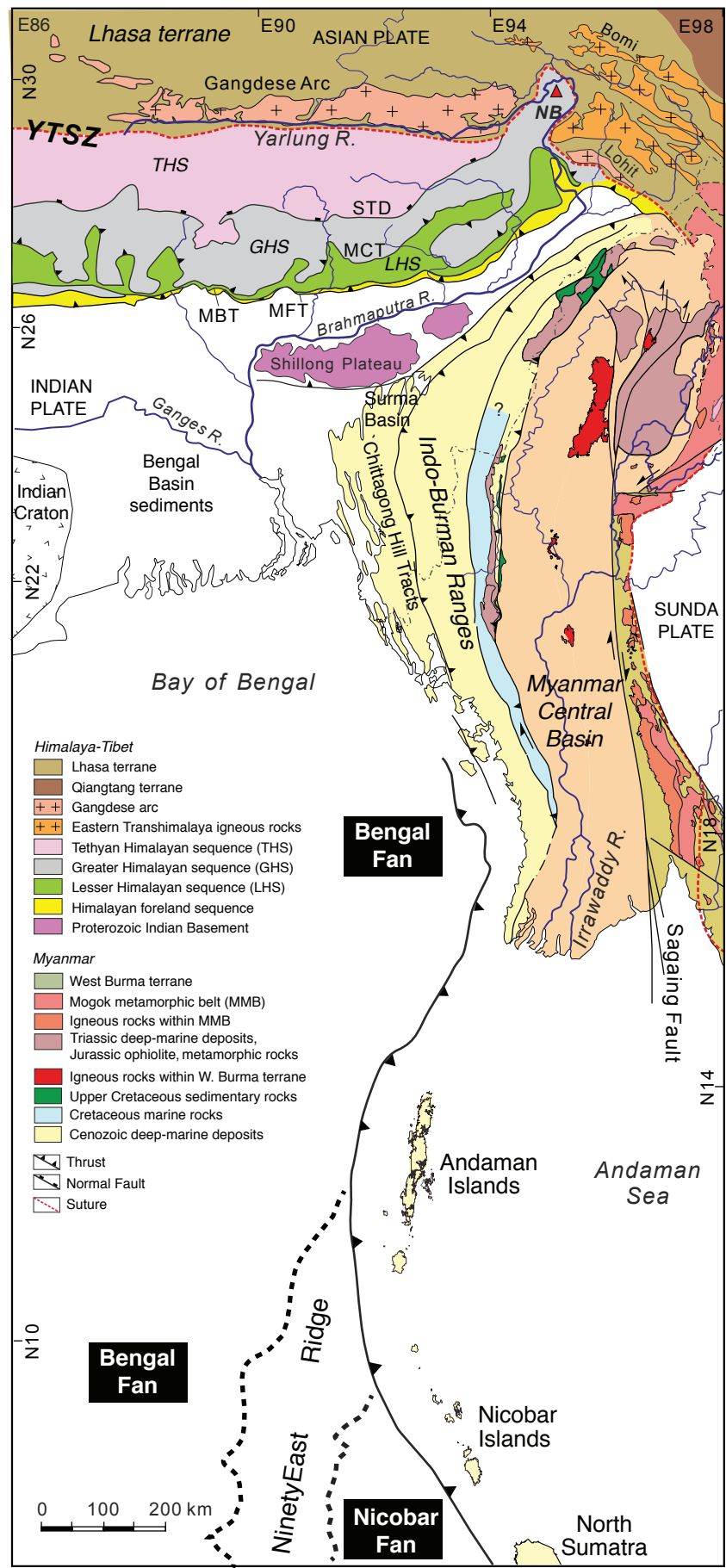


**Figure 3**

[Click here to download Figure: Fig3\\_Pickering et al.pdf](#)

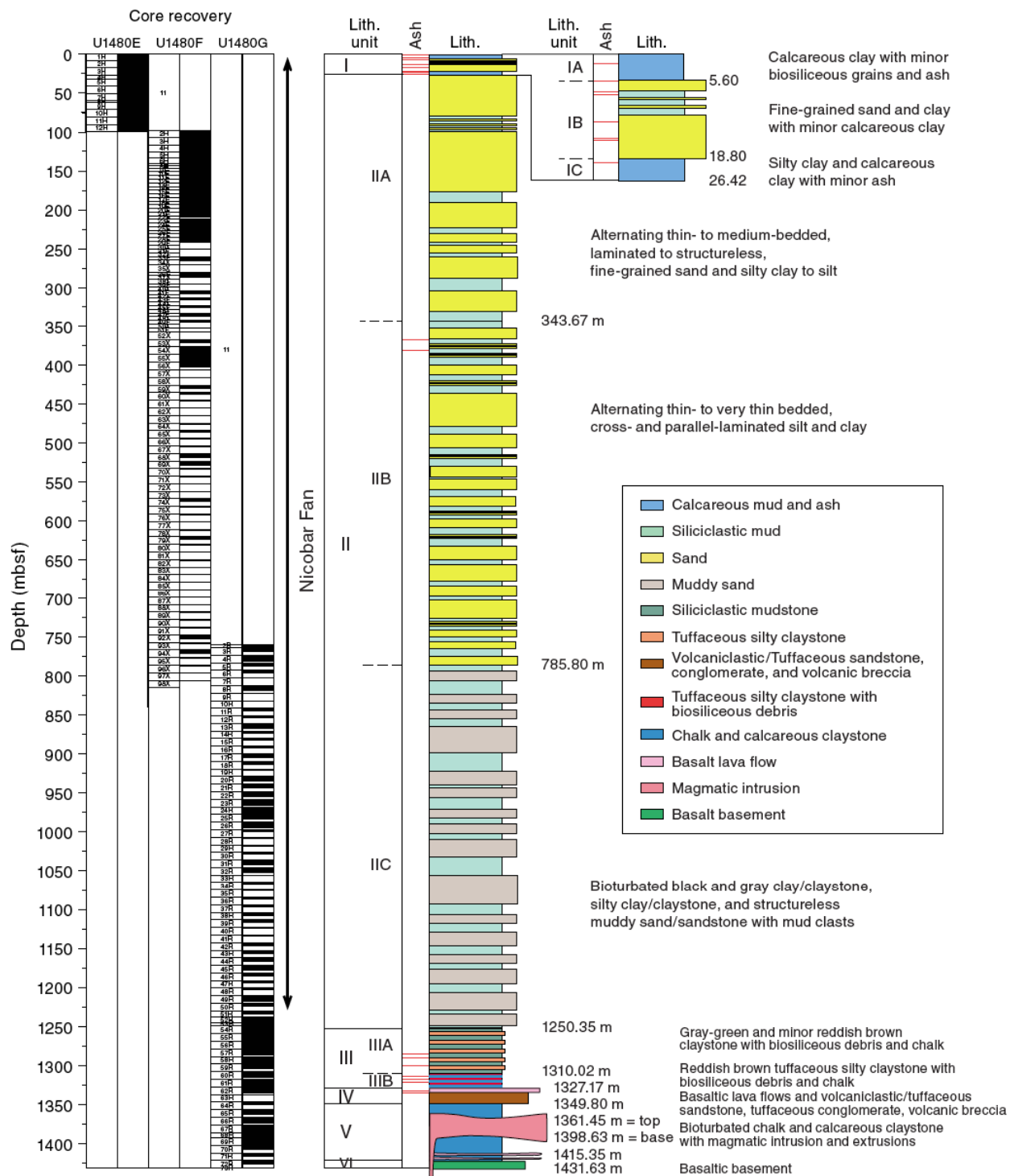
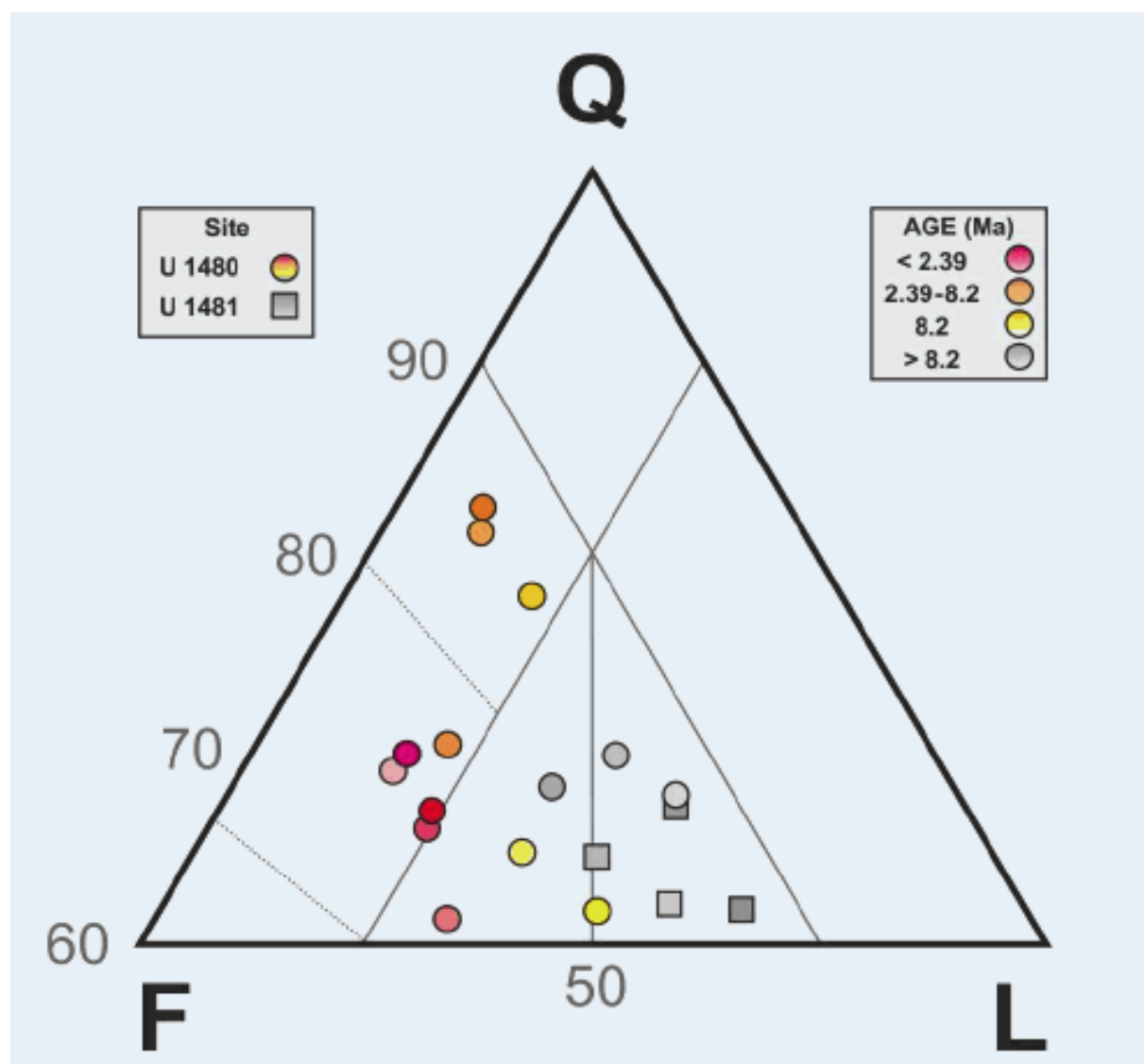
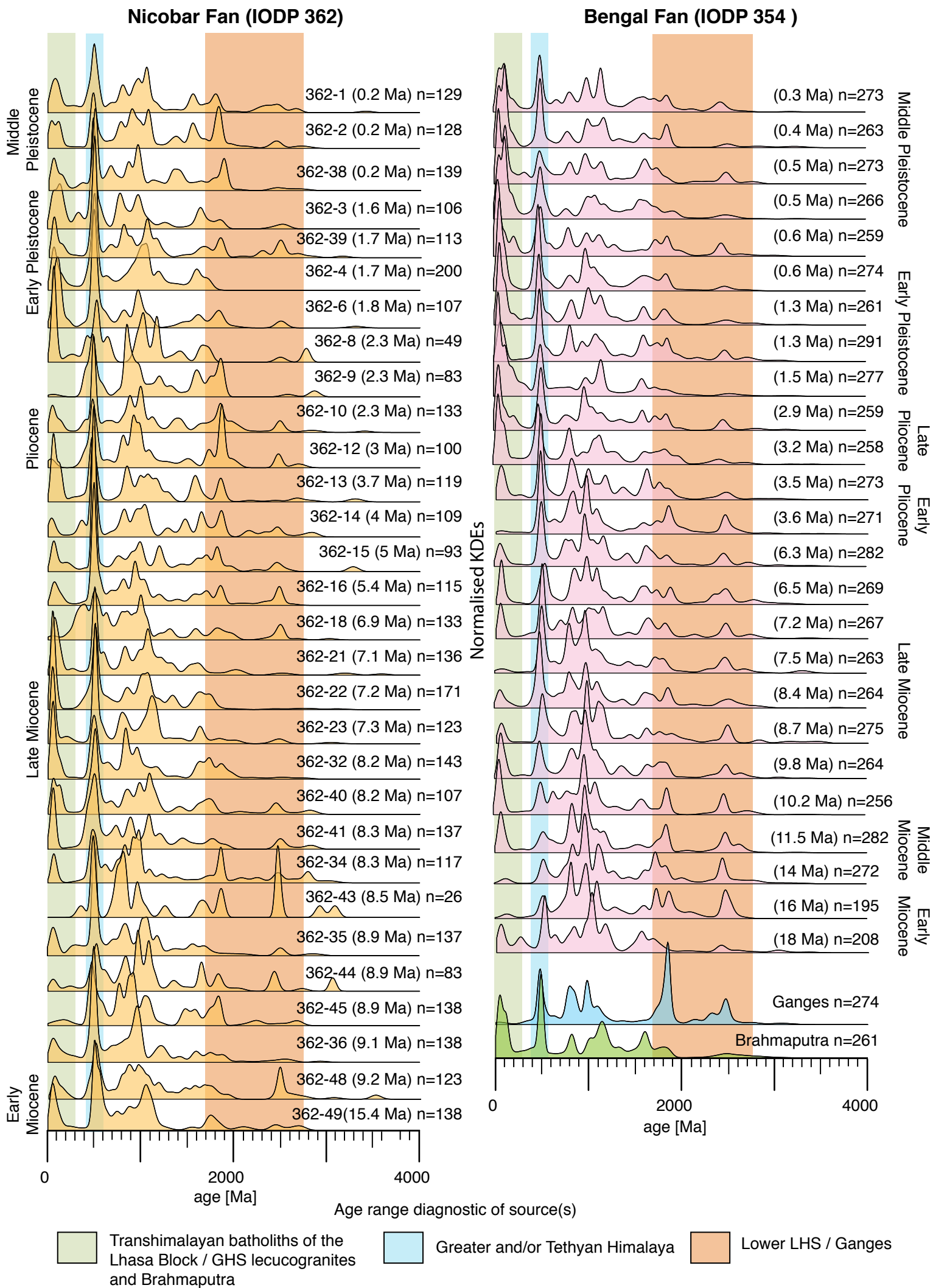


Figure 4  
[Click here to download Figure: Fig4\\_Pickering et al.pdf](#)



**Figure 5**  
[Click here to download Figure: Replacement Fig 5.pdf](#)



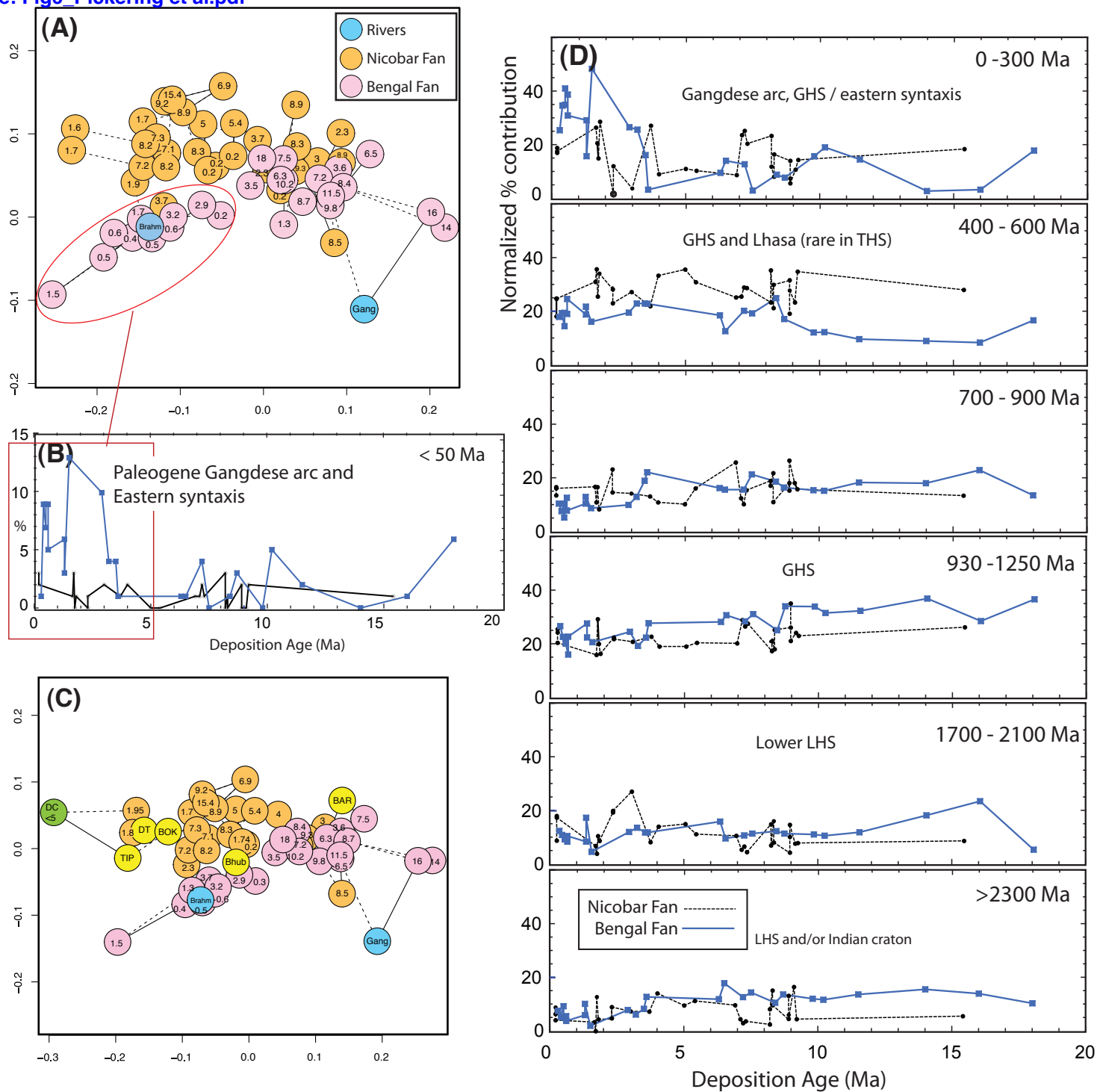
**Figure 6**[Click here to download Figure: Fig6\\_Pickering et al.pdf](#)

Figure 7  
[Click here to download Figure: Fig7\\_Pickering et al.pdf](#)

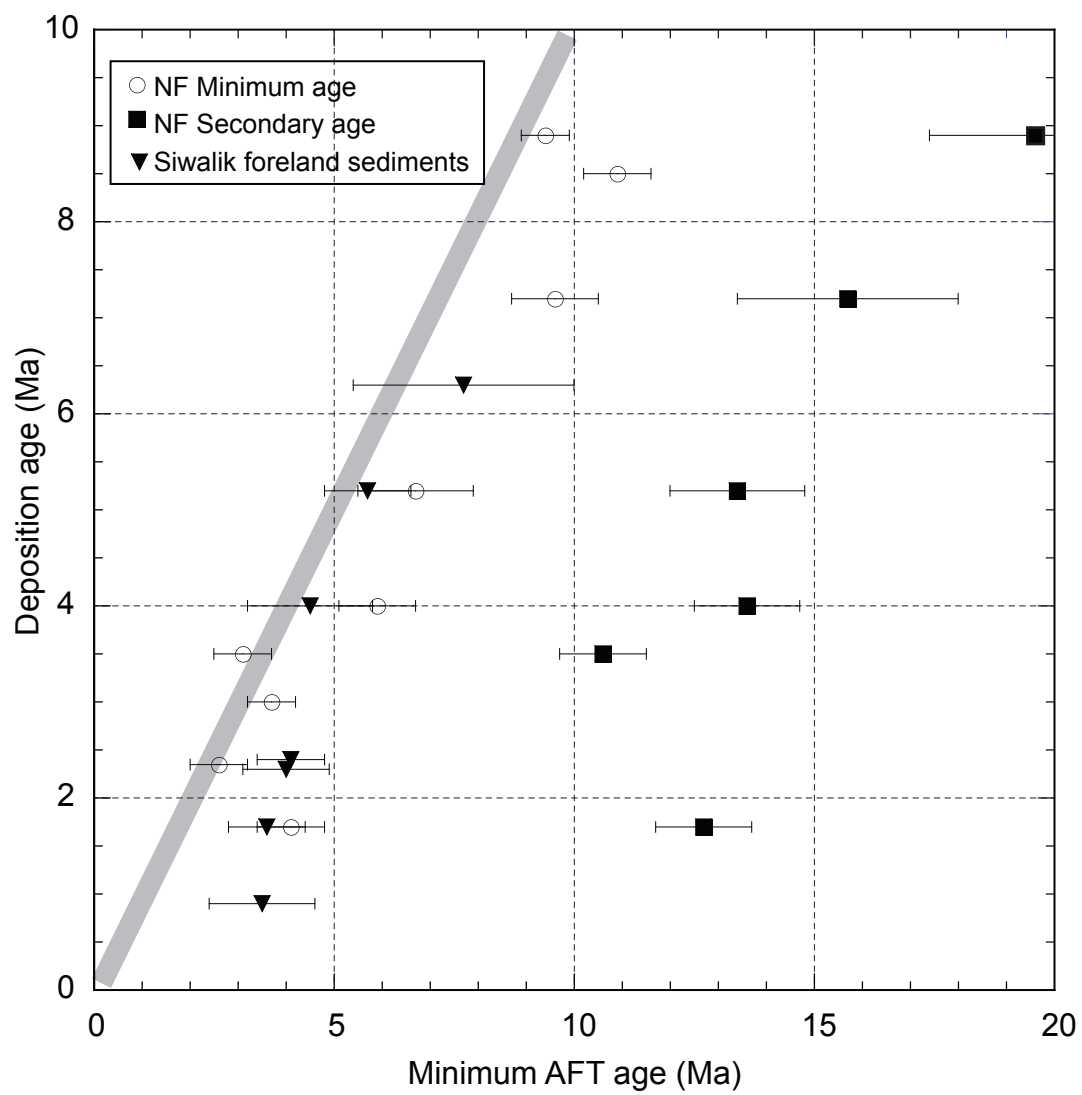


Figure 8

[Click here to download Figure: Fig8\\_Pickering et al.pdf](#)

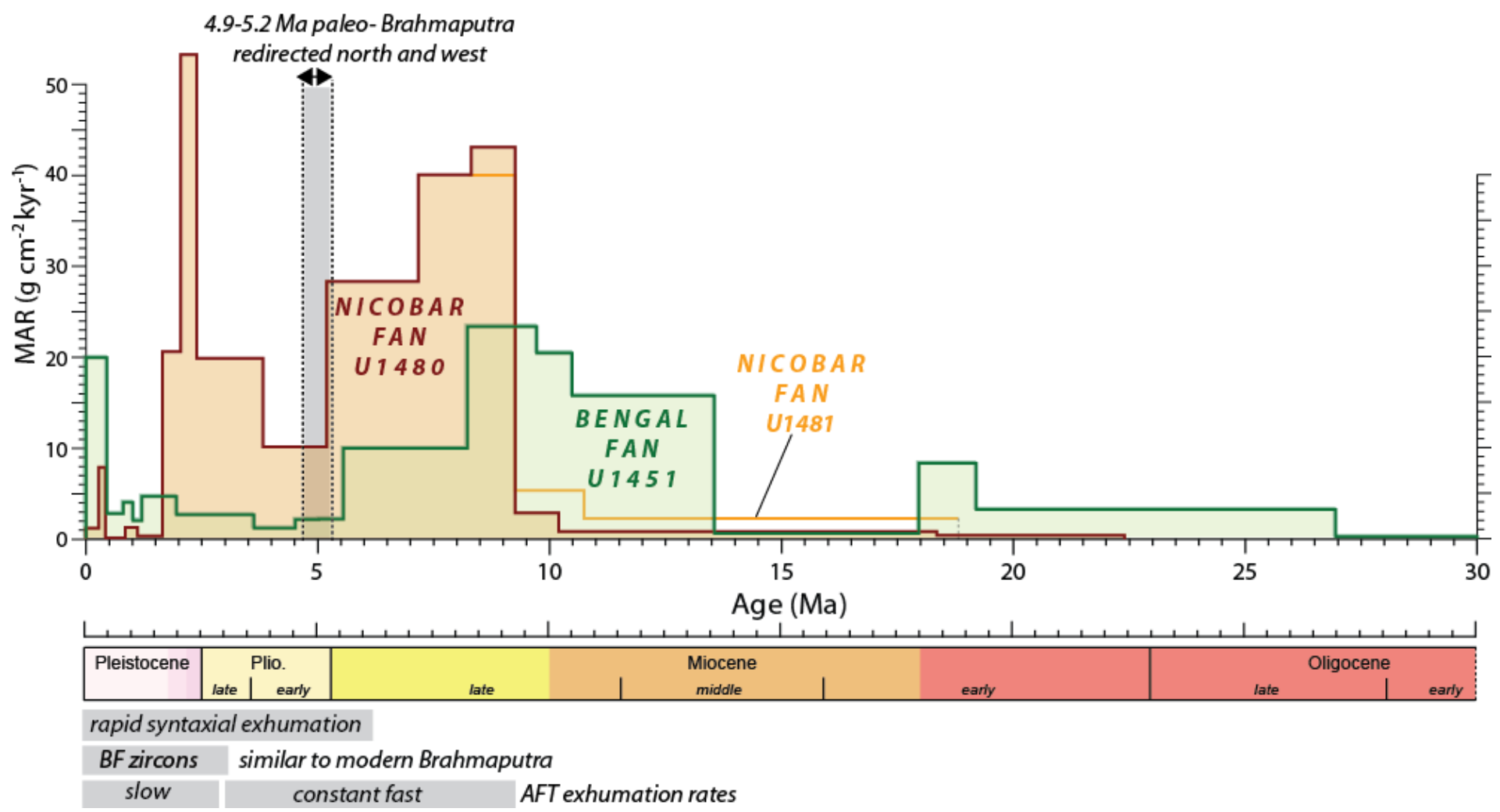


Figure 9

[Click here to download Figure: Fig9\\_Pickering et al.pdf](#)

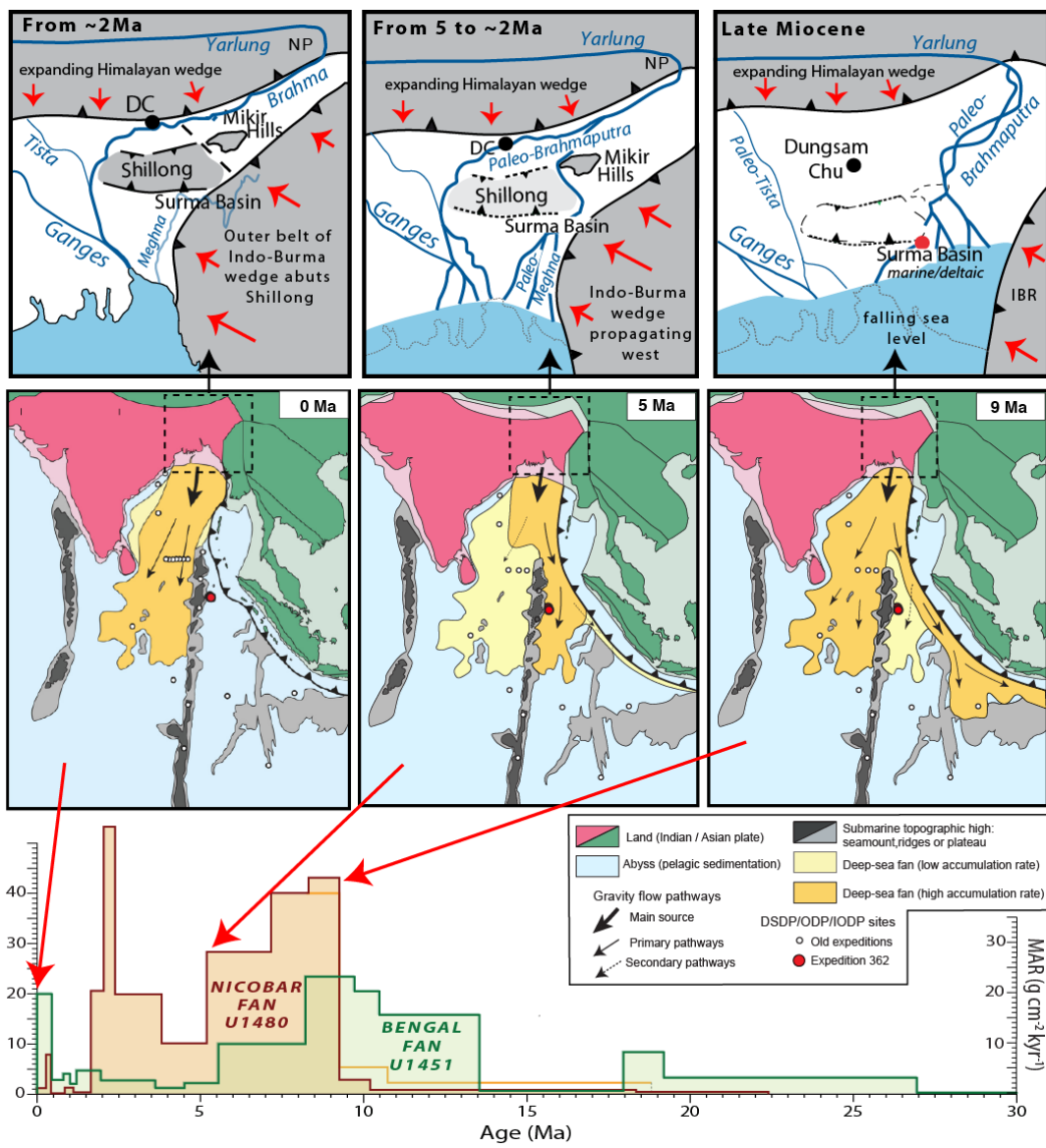


Table 1

[Click here to download Table: Table 1\\_Pickering et al 2019.doc](#)

Lab No	Deposit-ional Age	No. of grains	Central Age (Ma)	Age dispersion	Minimum Age (Ma)	Secondary Age (Ma)	Siwalik in Arunchal	Siwalik Eastern Bhutan
	<i>0.9</i>						3.5±1.1	
<i>362-3</i>	<i>1.6</i>	<i>66</i>	<i>7.1±0.9</i>	<i>56%</i>				
<i>362-4</i>	<i>1.7</i>	<i>30</i>	<i>4.8±0.8</i>	<i>84%</i>				
<i>362-39</i>	<i>1.7</i>	<i>50</i>	<i>5.2±0.7</i>	<i>68%</i>				
Combined	1.65	146	5.9±0.5	76%	4.1±0.7	12.7±1.1		3.6±0.8
<i>362-8</i>	<i>2.3</i>	<i>65</i>	<i>5.6±0.6</i>	<i>72%</i>			4.0±0.9	
<i>362-11</i>	<i>2.4</i>	<i>28</i>	<i>9.5±3.4</i>	<i>182%</i>				
Combined	2.35	93	7.0±1.1	138%	3.5±0.6			4.1±0.7
362-12	3.0	31	3.7±0.5	20%	3.7±0.5			
362-13	3.5	48	7.9±2.9	251%	3.1±0.6			
362-14	4.0	47	6.4±0.6	41%	5.9±0.8			4.5±1.3
<i>362-15</i>	<i>5.0</i>	<i>41</i>	<i>6.8±0.8</i>	<i>55%</i>				
<i>362-16</i>	<i>5.4</i>	<i>55</i>	<i>9.1±0.7</i>	<i>38%</i>				
Combined	5.2	96	8.2±0.6	47%	6.7±1.2	13.4±1.4		5.7±0.9
	<i>6.3</i>						7.7±2.3	
362-22	7.2	85	9.1±0.7	38%	9.6±0.9	15.7±2.3		
362-43	8.5	52	10.9±0.7	9%	10.9±0.7			
<i>362-35</i>	<i>8.9</i>	<i>45</i>	<i>8.9±0.6</i>	<i>8%</i>				
<i>362-44</i>	<i>8.9</i>	<i>21</i>	<i>9.0±1.1</i>	<i>7%</i>				
<i>362-45</i>	<i>8.9</i>	<i>50</i>	<i>9.5±0.9</i>	<i>44%</i>				
<i>362-46</i>	<i>9.0</i>	<i>61</i>	<i>11.8±1.0</i>	<i>36%</i>				
Combined	8.95	177	10.1±0.5	33%	9.4±0.6	19.6±2.6		